

## PAPER

[View Article Online](#)  
[View Journal](#) | [View Issue](#)Cite this: *J. Mater. Chem. A*, 2025, **13**, 36151***In situ* generation of the spinel structured FeCr<sub>2</sub>O<sub>4</sub> catalyst for CO<sub>2</sub>-assisted ethane oxidative dehydrogenation**Meng Du,<sup>a,b,c</sup> Bing Nan,<sup>a,b,\*</sup> Yunan Li,<sup>a,c</sup> Zhengwu Liu,<sup>a,c</sup> Kunming Hou,<sup>b</sup> Yulin Qin,<sup>b</sup> Guanhaojie Zheng,<sup>b</sup> Zhenye Liang,<sup>a,c</sup> Lina Zhang,<sup>b</sup> Daolei Wang,<sup>d</sup> Lingling Guo,<sup>b</sup> Luozhen Jiang,<sup>b</sup> Chen Tian,<sup>b</sup> Peng Fan,<sup>b</sup> Nannan Sun,<sup>b</sup> and Lina Li<sup>a,b,\*</sup>

Ethylene (C<sub>2</sub>H<sub>4</sub>) is a crucial raw material for the chemical industry. Recently, the oxidative dehydrogenation of ethane (C<sub>2</sub>H<sub>6</sub>) using CO<sub>2</sub> as a milder oxidant (CO<sub>2</sub>-ODHE) has been proposed as a potential method for C<sub>2</sub>H<sub>4</sub> production through the efficient utilization of shale gas and the mitigation of CO<sub>2</sub> emissions. In this work, a series of Fe, Cr–Fe, and Cr oxides were prepared by a two-step urea precipitation method with Fe<sub>3</sub>O<sub>4</sub>, FeCr<sub>2</sub>O<sub>4</sub>, and Cr<sub>2</sub>O<sub>3</sub> components, in which the Cr–Fe catalyst exhibits better activity with the conversion of ethane (35%) and CO<sub>2</sub> (27%) and stable C<sub>2</sub>H<sub>4</sub> yield (18%) at 650 °C. Through TEM, SEM, Raman, XAFS and *in situ* XRD results, it was found that the *in situ* formation of FeCr<sub>2</sub>O<sub>4</sub> during the CO<sub>2</sub>-ODHE reaction can enhance the thermostability of the Cr–Fe catalyst. Furthermore, the generated FeCr<sub>2</sub>O<sub>4</sub> effectively adsorbs and activates CO<sub>2</sub> molecules to reduce the generation of deposited carbon on the surface of the Cr–Fe catalyst.

Received 24th June 2025

Accepted 13th September 2025

DOI: 10.1039/d5ta05111h

[rsc.li/materials-a](https://rsc.li/materials-a)**1. Introduction**

Ethylene (C<sub>2</sub>H<sub>4</sub>) is recognized as the cornerstone of the petrochemical industry, serving as a crucial intermediate for over 70% of fundamental organic chemical raw materials, including ethylene oxide, polypropylene, and polystyrene, which are widely applied in textiles, plastics, and other fields.<sup>1,2</sup> With the recent continuous increase in verified shale gas reserves, the catalytic dehydrogenation of light alkanes, which constitute more than 20% of shale gas, has emerged as a promising and economically efficient pathway for ethylene production.<sup>3,4</sup> The oxidative dehydrogenation of ethane using CO<sub>2</sub> (CO<sub>2</sub>-ODHE) refers to the process with CO<sub>2</sub> as a mild oxidant to produce ethylene with lower energy consumption and a higher reaction equilibrium constant<sup>5</sup> and eliminate carbon deposition<sup>6</sup> by providing reactive oxygen species (\*O). CO<sub>2</sub> can react with coke deposited on the catalyst surface *via* the Boudouard reaction (CO<sub>2</sub> + C = 2CO), thus improving catalyst performance. Furthermore, taking into account both thermodynamic and kinetic factors, the CO<sub>2</sub>-ODHE process needs to be conducted at high temperatures (>873 K), which results in several problems

such as poor thermal stability, susceptibility to sintering,<sup>7</sup> and carbon deposition, hindering its industrial applications.<sup>8</sup> However, the sintering of the active species at high reaction temperatures can lead to irreversible deactivation of the catalysts.<sup>9</sup> In addition, the side reactions, such as the reforming reaction and the reverse water–gas shift (RWGS) reaction, can significantly influence the overall catalytic performance. The reforming reaction with the conversion of alkanes into syngas (CO and H<sub>2</sub>) competes with the desired dehydrogenation pathway, leading to reduced ethylene selectivity and yield.<sup>10</sup> On the other hand, the RWGS reaction (CO<sub>2</sub> + H<sub>2</sub> ↔ CO + H<sub>2</sub>O) can promote the reaction equilibrium by consuming H<sub>2</sub>.<sup>5</sup> Therefore, developing efficient catalysts with excellent catalytic performance, sintering resistance, and anti-coking properties for the CO<sub>2</sub>-ODHE reaction has received wide research attention for both academic and practical significance.

Recently, a series of typical non-noble metal CO<sub>2</sub>-ODHE catalysts have been widely developed, such as Cr-, Ga-, and Fe-based oxides.<sup>5,11–15</sup> Chromium-based catalysts are the most widely studied active components in this field in the CO<sub>2</sub>-ODHE reaction because of their high activity and selectivity, which can make a recycle between metallic and oxidized Cr species to adsorb and activate CO<sub>2</sub> for the dehydrogenation of C<sub>2</sub>H<sub>6</sub>.<sup>16</sup> Both the inevitable toxicity of Cr<sup>6+</sup> and the easy aggregation of Cr<sub>2</sub>O<sub>3</sub> further restrict the application of Cr-based catalysts in the CO<sub>2</sub>-ODHE reaction.<sup>17</sup> In addition, Fe, as a typical promoter, is frequently used to modify active metals (Cr, Co, or Ni) by altering electronic and coordination structures. Yan *et al.*<sup>18</sup>

<sup>a</sup>Shanghai Institute of Applied Physics, Chinese Academy of Sciences, Shanghai 201204, China. E-mail: lilina@sinap.ac.cn<sup>b</sup>Shanghai Advanced Research Institute, Chinese Academy of Sciences, Shanghai 201210, China. E-mail: sunnn@sari.ac.cn; nanb@sari.ac.cn<sup>c</sup>University of Chinese Academy of Sciences, Beijing 100049, China<sup>d</sup>Division of China, TILON Group Technology Limited, Shanghai, China

found that the Ni-FeO<sub>x</sub> interface sites can selectively break C-H rather than C-C bonds in C<sub>2</sub>H<sub>6</sub> to promote the formation of C<sub>2</sub>H<sub>4</sub>. Furthermore, the Fe<sup>3+</sup>/Fe<sup>2+</sup> redox cycle and unique  $\alpha$ -Fe component can also effectively prevent reforming reactions.<sup>19</sup> Recently, FeCr<sub>2</sub>O<sub>4</sub> with a unique spinel structure has received wide attention because of its good conductivity, reducibility, and thermodynamic stability, and has been evidenced as an excellent participant in high-temperature reactions.<sup>9,20</sup> Besides, according to kinetic experimental and DFT studies, FeCr<sub>2</sub>O<sub>4</sub> could activate the sp<sup>2</sup> C-H bond of benzene with a lower activation energy compared to the Cr<sub>2</sub>O<sub>3</sub> component.<sup>21</sup> Bogdan *et al.* studied carbon-supported Fe-Cr-Ni and Fe-Cr oxide catalysts, discovering that the formation of the FeCr<sub>2</sub>O<sub>4</sub> phase on the surface of Fe-Cr/C catalysts is responsible for the high stability and high ethylene selectivity at 700 °C.<sup>22-24</sup> And in another study, they found that the formation of FeCr<sub>2</sub>O<sub>4</sub> could prevent the reduction of iron and the formation of iron carbides.<sup>25</sup> Additionally, in their latest research, it was found that a reversible water-gas shift reaction is activated by spinel-type oxide phases, which was characterized in detail by *in situ* magnetometry and Mössbauer spectroscopy methods.<sup>26</sup> While these studies highlight the beneficial role of the supported FeCr<sub>2</sub>O<sub>4</sub> phase, the potential for its *in situ* generation during the demanding CO<sub>2</sub>-ODHE reaction itself, and its subsequent impact on catalytic performance and stability, remain less explored. Thus, we investigate the structural evolution of FeCr oxide catalysts under CO<sub>2</sub>-ODHE conditions, specifically focusing on whether the beneficial FeCr<sub>2</sub>O<sub>4</sub> spinel phase forms *in situ* during the reaction and how this dynamic process governs catalytic behavior.

Here, we synthesized nano-iron oxide, chromium oxide, and FeCr bimetallic oxides using a two-step urea precipitation method and applied them in the CO<sub>2</sub>-ODHE reaction. Through a series of structural characterization studies such as XRD, SEM, TEM, Raman, XAFS, and temperature-programmed experiments, we found that the spinel structured FeCr<sub>2</sub>O<sub>4</sub>, which is formed *in situ* under the reaction atmosphere, exhibited good thermal stability to endure the high reaction temperature. Meanwhile, FeCr<sub>2</sub>O<sub>4</sub> could enhance the adsorption and activation of CO<sub>2</sub> to mitigate coke accumulation and improve the activity.

## 2. Experimental

### 2.1. Catalyst preparation

Without any additional purification, all of the chemicals utilized in this work were of analytical grade and bought from Sinopharm Chemical Reagent Co., Ltd.

The catalysts used in this study were synthesized using a two-step urea hydrolysis co-precipitation method. Ferric nitrate (Fe(NO<sub>3</sub>)<sub>3</sub>·9H<sub>2</sub>O) and chromium nitrate (Cr(NO<sub>3</sub>)<sub>3</sub>·9H<sub>2</sub>O) were chosen as the metal precursors. The metal ion ratios were controlled at 1 : 0, 1 : 3, and 0 : 1, respectively. The metal nitrates were mixed, stirred, and dissolved in deionized water. The mixture was aged for 1 h and then transferred to a 100 mL polytetrafluoroethylene (PTFE)-lined autoclave. The autoclave was first maintained at 80 °C in an oven for 6 h and then heated to 180 °C for 24 h. Afterward, the autoclave was allowed to cool

naturally to room temperature. The resulting precipitates were collected by multiple centrifugations and washed with deionized water until the pH reached 7. The final products were dried in a vacuum oven at 70 °C and then calcined at 400 °C for 4 h with a heating rate of 10 °C min<sup>-1</sup>. The fresh samples obtained were designated as Fe, Cr-Fe, and Cr, respectively.

### 2.2. Characterization

The nitrogen adsorption-desorption isotherm was recorded on an ASAP2020-HD88 analyzer (Micromeritics Co., Ltd.) at 77 K. Before introducing N<sub>2</sub>, the measured powders were degassed at 250 °C for 4 h under vacuum (<100 μm Hg). The pore-size distribution of each sample was calculated using the BJH method in accordance with the desorption branch of the obtained isotherms. The BET specific surface areas were calculated from data in the relative pressure range between 0.06 and 0.30.

The powder X-ray diffraction (XRD) patterns were obtained using Cu K<sub>α1</sub> radiation ( $\lambda = 1.540598 \text{ \AA}$ ) with a scanning range of 10°–90° on a Panalytical Empyrean X-ray diffractometer (40 kV and 40 mA). Prior to each test, the ground sample was planished on a quartz sample holder.

The transmission electron microscopy (TEM), high-resolution transmission electron microscopy (HRTEM) and scanning transmission electron microscopy-energy dispersive spectrometry (STEM-EDS) elemental mapping images were recorded on an FEI TALOS F200X microscope with an acceleration voltage of 200 kV. The measured samples were first ultrasonically dispersed in pure alcohol for about 5 min, and then a drop of the liquid supernatant was applied to a very thin carbon film. Before being placed inside the sample holder, the sample grid was allowed to dry naturally. The scanning electron microscope (SEM) images were obtained from a field emission scanning electron microscope (Zeiss, Sigma 500).

X-ray photoelectron spectroscopy (XPS) for the used samples was performed by using a PHI 5000 Versa Probe III with a monochromatic Al K<sub>α</sub> X-ray source with a beam size of 100 μm × 1400 μm. Charge compensation was achieved by dual beam charge neutralization and the binding energy was corrected by setting the binding energy of the hydrocarbon C 1s feature to 284.8 eV.

The Raman spectra were collected using a Renishaw Raman InVia reflex microscope with laser excitation at 532 nm. The samples were attached to a glass slide, and Raman shifts were acquired from 100 to 1900 cm<sup>-1</sup> with a spectral resolution of 1 cm<sup>-1</sup>. For each experimental run, the scanning parameter for each Raman spectrum was set at 100 s in order to improve the signal-to-noise ratio. In order to assess the repeatability of the spectral results, several spot analyses were performed on various regions of the same sample.

The X-ray absorption fine structure (XAFS) spectra at the Fe K-edge ( $E^0 = 7112 \text{ eV}$ ) and Cr K-edge ( $E^0 = 5989 \text{ eV}$ ) were recorded at BL14W1 and 16U1 beam lines of Shanghai Synchrotron Radiation Facility (SSRF) operated at 3.5 GeV in “top-up” mode with a constant current of 220 mA. The XAFS data were recorded in transmission mode. The energy was calibrated according to the



absorption edge of pure Fe and Cr foil. The data were analyzed using the Demeter software package.<sup>27</sup> For the X-ray absorption near edge structure (XANES) part, the experimental absorption coefficients as a function of energies  $\mu(E)$  were processed by background subtraction and normalization procedures, and reported as “normalized absorption”. The chemical valence of Fe was determined with the linear combination fit by comparison to the corresponding references of Fe/Fe<sub>3</sub>O<sub>4</sub> based on the normalized XANES profiles in the Athena software. For the extended X-ray absorption fine structure (EXAFS) part, the Fourier transformed (FT) data in *R* space were analyzed by multiple Fe compound models for Fe–O, Fe–O–Fe or Fe–O–Cr shells, respectively. The passive electron factors,  $S_0^2$ , were determined by fitting the experimental Fe foil data and fixing the Fe–Fe coordination number (CN) to be 8 + 6, and then fixed for further analysis of the measured samples. For Cr, the Fourier transform (FT) in *R*-space is analyzed by applying Cr<sub>2</sub>O<sub>3</sub> and Cr<sub>2</sub>FeO<sub>4</sub> models to Cr–O and Cr–O–Cr, respectively. Similarly, amp was obtained by fixing the coordination number (CN) of Cr–Cr as 6 according to the data of Cr foil, and then  $S_0^2$  was fixed to further analyze the measured samples. The parameters describing the electronic properties (e.g., correction to the photoelectron energy origin,  $E^0$ ) and local structure environment including the coordination number (CN), bond distance (*R*) and Debye–Waller (D.W.) factor around the absorbing atoms were allowed to vary during the fitting process. The fitted ranges for *k* were selected to be  $k = 3.0\text{--}12.0 \text{ \AA}^{-1}$  and  $2.8\text{--}11.0 \text{ \AA}^{-1}$  ( $k^3$  weighted) for Fe and Cr samples, respectively. The Fourier transformed (FT) data in *R* space were analyzed by selecting  $R = 1.0\text{--}3.4$  and  $1.2\text{--}3.0 \text{ \AA}$  ( $k^3$  weighted), respectively.

*In situ* X-ray diffraction (XRD) measurements of Cr–Fe catalysts were carried out within a compact flow cell at the BL02U2 beam line of Shanghai Synchrotron Radiation Facility (SSRF) ( $\lambda = 0.79743 \text{ \AA}$ ). Two-dimensional XRD data were acquired by using a Pilatus 2M with a distance of *c.a.* 240 mm from the samples. The catalyst sample was compressed into a disc with a diameter of 10 mm and then placed on the heating stage of the *in situ* cell. It was reduced *in situ* by a mixture of H<sub>2</sub>/Ar (20/20 mL min<sup>−1</sup>) with the temperature ramping from room temperature to 450 °C (40 °C min<sup>−1</sup>) and holding for 30 min. After flushing in Ar for 10 min, the catalyst was sequentially exposed to the reaction gases (CO<sub>2</sub>/C<sub>2</sub>H<sub>6</sub>/Ar = 10/10/20 mL min<sup>−1</sup>), and then the temperature was increased to 500, 600, 650, and 700 °C (10 °C min<sup>−1</sup>), respectively. Each temperature point was maintained for 15 min. The two-dimensional (2D) diffraction images were continuously collected by using a Pilatus3 S-2M detector. The LaB<sub>6</sub> standard was used for wavelength calibration. The 2D images were subsequently integrated using the program Dioplas to obtain XRD profiles. The  $2\theta$  angle was converted to the corresponding value of the Cu K $\alpha_1$  radiation ( $\lambda = 1.54056 \text{ \AA}$ ).

The temperature-programmed reduction by hydrogen (H<sub>2</sub>-TPR) measurements for the catalyst samples were conducted on a Micromeritics AutoChem II 2920 instrument equipped with a thermal conductivity detector (TCD). After being pretreated under O<sub>2</sub> (5% O<sub>2</sub>/He) flow in a quartz U-tube reactor at 300 °C for 30 min, the samples (50 mg) were cooled down to room temperature in Ar. Then 5% H<sub>2</sub>/Ar (50 mL min<sup>−1</sup>) was introduced to pass through the catalyst bed until a stable TCD signal was observed.

Subsequently, a temperature ramping program from room temperature to 800 °C at the rate of 10 °C min<sup>−1</sup> was performed.

CO<sub>2</sub>-temperature programmed desorption (CO<sub>2</sub>-TPD) was carried out on an AutoChem II 2920 (Micromeritics, USA) instrument and a mass spectrometer (LC-D200M, TILON) was used to gather gas signals. 100 mg of fresh catalyst was placed in a U-shaped quartz sample tube. Prior to TPD studies, the catalyst sample was processed with 5% H<sub>2</sub>/Ar (50 mL min<sup>−1</sup>) at 450 °C for 90 min and then cooled down to room temperature using the same steam. He was purged for 30 min and then the catalyst was exposed to 5% CO<sub>2</sub>/He (50 mL min<sup>−1</sup>) for 1 h until surface saturation was achieved. The weakly physisorbed CO<sub>2</sub> was purged by flushing in He (50 mL min<sup>−1</sup>) for 30 min. Finally, desorption of CO<sub>2</sub> was carried out by increasing the temperature to 700 °C at a ramp of 10 °C min<sup>−1</sup> under He. The signals of He ( $m/z = 4$ ) and CO<sub>2</sub> ( $m/z = 44$ ) were detected by using the mass spectrometer during the investigation.

CO<sub>2</sub>-temperature programmed surface reaction (CO<sub>2</sub>-TPSR) experiments were performed to prove the oxidation of deposited carbon by CO<sub>2</sub> for used catalysts (85 mg) on a similar instrument to CO<sub>2</sub>-TPD. After being pretreated under He (30 mL min<sup>−1</sup>) in a quartz U-tube reactor at 150 °C for 30 min, the samples were cooled down to room temperature in He. Then 5% CO<sub>2</sub>/He (30 mL min<sup>−1</sup>) was introduced to pass through the catalyst bed until a stable TCD signal was observed. Subsequently, a temperature ramping program from room temperature to 900 °C at a rate of 10 °C min<sup>−1</sup> was performed under 5% CO<sub>2</sub>/He flow. The signals of He ( $m/z = 4$ ) and CO<sub>2</sub> ( $m/z = 44$ ) were detected by using the mass spectrometer during the investigation. He-TPSR experiments were conducted to prove the intrinsic active oxygen species for coke elimination of the used catalysts (50 mg), following the same procedure as the CO<sub>2</sub>-TPSR experiments, with the only difference being that the CO<sub>2</sub> flow was replaced by a He flow.

The TPO experiment was performed using a thermoanalyzer (Setaram Labsys Evo 1150) coupled with a mass spectrometer for evolved gas analysis to quantify the amount of coke deposited on the used catalysts after CO<sub>2</sub>-ODHE at 700 °C. The ~10 mg catalyst was placed in a 70  $\mu$ L alumina crucible and heated at 40–800 °C (5 °C min<sup>−1</sup>) under 20% O<sub>2</sub>/N<sub>2</sub> flow (40 mL min<sup>−1</sup>). The amount of CO<sub>2</sub> in the outlet gas was quantified by using an online mass spectrometer.

### 2.3. Catalytic tests

The catalytic performance of the samples in CO<sub>2</sub>-ODHE was evaluated in a 6 mm fixed-bed micro-reactor. 100 mg of catalyst was used in each test. The catalyst was fixed in the middle of the bed with quartz cotton, and the reaction temperature of the catalyst was monitored by a thermocouple located in the center of the bed. Before the catalytic performance test, the catalysts were pretreated at 450 °C in a 50% H<sub>2</sub>/Ar flow for 1 hour, and then the reaction was initiated by feeding a mixture gas with C<sub>2</sub>H<sub>6</sub>/CO<sub>2</sub>/Ar = 10 : 10 : 20 mL min<sup>−1</sup> under atmospheric pressure, with N<sub>2</sub> being used as the internal standard. The reaction temperature ranged from 500 to 700 °C, with a step increment of 50 °C. Each temperature point was maintained for 40 min to ensure the reliability and repeatability of the gas chromatography data, allowing



us to obtain activity data for the catalysts at different temperatures. The samples after the reaction were designated as Fe-used, Cr-Fe-used, and Cr-used, respectively.

The reaction products were analyzed by using a gas chromatograph (Agilent Technologies 7890B), using a flame ionization detector (FID) equipped with an alumina capillary column to detect CH<sub>4</sub>, C<sub>2</sub>H<sub>6</sub>, and C<sub>2</sub>H<sub>4</sub> (N<sub>2</sub> carrier gas) and a thermal conductivity detector (TCD) packed with Porapak Q columns, N columns and molecular sieve 5 A columns to detect H<sub>2</sub>, N<sub>2</sub>, CO, CH<sub>4</sub>, and CO<sub>2</sub> (He carrier gas). C<sub>2</sub>H<sub>6</sub> conversion ( $X(\text{C}_2\text{H}_6)$ ), CO<sub>2</sub> conversion ( $X(\text{CO}_2)$ ), C<sub>2</sub>H<sub>4</sub> yield ( $Y(\text{C}_2\text{H}_4)$ ), C<sub>2</sub>H<sub>4</sub> selectivity ( $S(\text{C}_2\text{H}_4)$ ), CO selectivity ( $S(\text{CO})$ ) and CH<sub>4</sub> selectivity ( $S(\text{CH}_4)$ ) in gaseous products and carbon balance are calculated as follows:

$$X(\text{C}_2\text{H}_6) = [F(\text{C}_2\text{H}_6, \text{in}) - F(\text{C}_2\text{H}_6, \text{out})]/F(\text{C}_2\text{H}_6, \text{in}) \times 100\%,$$

$$X(\text{CO}_2) = [F(\text{CO}_2, \text{in}) - F(\text{CO}_2, \text{out})]/F(\text{CO}_2, \text{in}) \times 100\%,$$

$$Y(\text{C}_2\text{H}_4) = F(\text{C}_2\text{H}_4, \text{out})/F(\text{C}_2\text{H}_6, \text{in}) \times 100\%,$$

$$S(\text{C}_2\text{H}_4) = Y(\text{C}_2\text{H}_4)/X(\text{C}_2\text{H}_6) \times 100\%,$$

$$S_{\text{gas}}(\text{C}_2\text{H}_4) = 2 \times F(\text{C}_2\text{H}_4, \text{out})/[2 \times F(\text{C}_2\text{H}_4, \text{out}) + F(\text{CO}, \text{out}) + F(\text{CH}_4, \text{out})] \times 100\%,$$

$$S_{\text{gas}}(\text{CH}_4) = F(\text{CH}_4, \text{out})/[2 \times F(\text{C}_2\text{H}_4, \text{out}) + F(\text{CO}, \text{out}) + F(\text{CH}_4, \text{out})] \times 100\%,$$

$$S_{\text{gas}}(\text{CO}) = F(\text{CO}, \text{out})/[2 \times F(\text{C}_2\text{H}_4, \text{out}) + F(\text{CO}, \text{out}) + F(\text{CH}_4, \text{out})] \times 100\%,$$

$$\begin{aligned} \text{Carbon balance} = & [2 \times F(\text{C}_2\text{H}_6, \text{out}) + 2 \times F(\text{C}_2\text{H}_4, \text{out}) \\ & + F(\text{CH}_4, \text{out}) + F(\text{CO}_2, \text{out}) \\ & + F(\text{CO}, \text{out})]/[2 \times F(\text{C}_2\text{H}_6, \text{in}) \\ & + F(\text{CO}_2, \text{in})] \times 100\%, \end{aligned}$$

where  $F(i, \text{in})$  and  $F(i, \text{out})$  stand for the volume flow of component  $i$  (mL min<sup>-1</sup>) after N<sub>2</sub> correction at the inlet and outlet, respectively.

$$F(i) = F(\text{N}_2) \times A(i)/A(\text{N}_2) \times R(i)/R(\text{N}_2)$$

where  $A(i)$  is the peak area of component  $i$  in the gas chromatogram and  $R(i)$  is the relative response factor of component  $i$  (determined by calibration with standard gases).

In the comparison of ethylene formation rates, the effects of space velocity and inert gas dilution have been excluded using the following calculation formula:

$$\text{Rates of ethylene formation } (\mu\text{mol g}_{\text{cat}}^{-1} \text{ s}^{-1}) = Y(\text{C}_2\text{H}_4) \times \text{space velocity (GHSV)} \times (V_{\text{C}_2\text{H}_6}/V_{\text{total}})/V_{\text{m}}$$

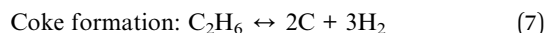
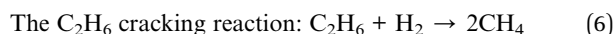
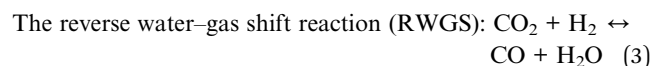
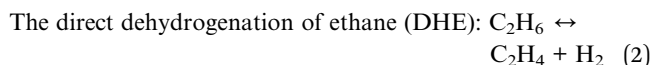
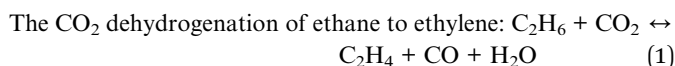
### 3. Results and discussion

#### 3.1. CO<sub>2</sub>-ODHE catalytic reaction performance

In this work, a series of monometallic and bimetallic iron-chromium oxide catalysts were evaluated by a CO<sub>2</sub>-assisted

ethane dehydrogenation reaction. Typically, the catalytic performance of samples with different Cr/Fe ratios was tested to optimize the catalyst (Fig. S1). The Cr-Fe (3 : 1) sample with the highest ethylene yield was selected for comparison with monometallic samples to investigate the structure-activity relationship.

During the CO<sub>2</sub>-ODHE, C<sub>2</sub>H<sub>4</sub>, CH<sub>4</sub>, CO, H<sub>2</sub>, H<sub>2</sub>O, and C products are formed according to the following reactions:<sup>18,28,29</sup>



The main and side reactions collectively determine the overall material balance and reaction activity. The results of catalytic experiments and the mass ratio of products at 650 °C are shown in Fig. 1 and Table S1. As the temperature increased, the Cr-Fe bimetallic sample exhibited much better activity compared with the monometallic Fe and Cr samples. At 650 °C, the conversion of ethane and CO<sub>2</sub> approached 35% and 27%, respectively. The product mass content, with CO constituting 61% and ethylene accounting for 23%, while coke formation representing only 5%, indicates that the Cr-Fe sample is a promising catalyst for the ethane oxidative dehydrogenation reaction. Although the monometallic Cr catalyst exhibited 20% for ethane conversion at 650 °C, consistent with unsupported Cr-based catalysts even at a lower space velocity of 3600 mL g<sub>cat</sub><sup>-1</sup> h<sup>-1</sup>,<sup>7,12</sup> both the CO<sub>2</sub> conversion and ethylene yield were significantly lower compared to the Cr-Fe catalyst. Additionally, the significant amount of coke deposited on the monometallic Cr catalyst (accounting for 66% of the mass content) clearly indicates the rapid occurrence of coke formation under high-temperature conditions. Meanwhile, the monometallic Fe catalyst exhibited poor catalytic performance in the CO<sub>2</sub>-ODHE reaction, only achieving the conversion of both C<sub>2</sub>H<sub>6</sub> and CO<sub>2</sub> below 5%, which demonstrated the poor ability to activate the C-H and C-O bonds even at such a high temperature of about 650 °C. Supported monometallic Fe-based catalysts in previous studies, such as Fe/CeO<sub>2</sub> and Fe/MoO<sub>3</sub>, exhibit very low ethane conversion of only 0.5%<sup>18</sup> and 8%<sup>30</sup> at 600 °C, respectively. Carbon balance for all the experiments reached above 95% except for the monometallic Cr catalysts at 650 °C, which reached only 89% (Fig. 2), and no C3, C4, or aromatics were detected. Since the formation of coke is related to the reaction





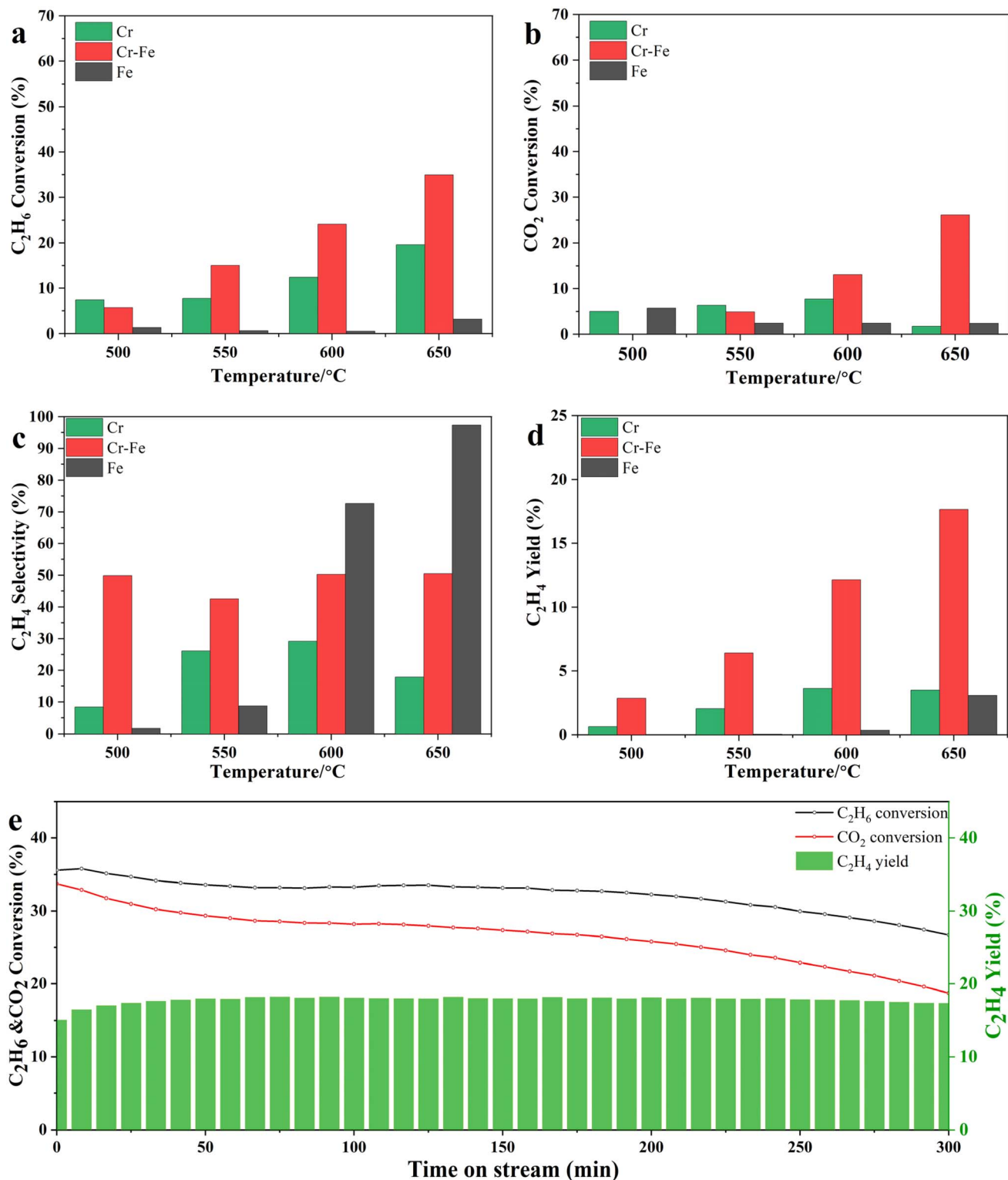


Fig. 1 Catalytic performance of the CO<sub>2</sub>-ODHE reaction of Cr, Cr-Fe, and Fe. (a) C<sub>2</sub>H<sub>6</sub> conversion, (b) CO<sub>2</sub> conversion, (c) C<sub>2</sub>H<sub>4</sub> selectivity, (d) C<sub>2</sub>H<sub>4</sub> yield, and (e) stability at 650 °C of Cr-Fe samples (space velocity: 24 000 mL g<sub>cat</sub><sup>-1</sup> h<sup>-1</sup>).

time, we calculated the selectivity of C<sub>2</sub>H<sub>4</sub>, CO, and CH<sub>4</sub> in the gas-phase products as the temperature increased for different catalyst samples based on the carbon balance data, as shown in Fig. 2. At the initial temperature of 500 °C, the ethylene

selectivity of the Cr-Fe bimetallic oxide sample was about 56.7%, with low conversion of C<sub>2</sub>H<sub>6</sub> and CO<sub>2</sub>. As the conversion increased with temperature, the ethylene selectivity in gas-phase products decreased to 40% at 650 °C due to the



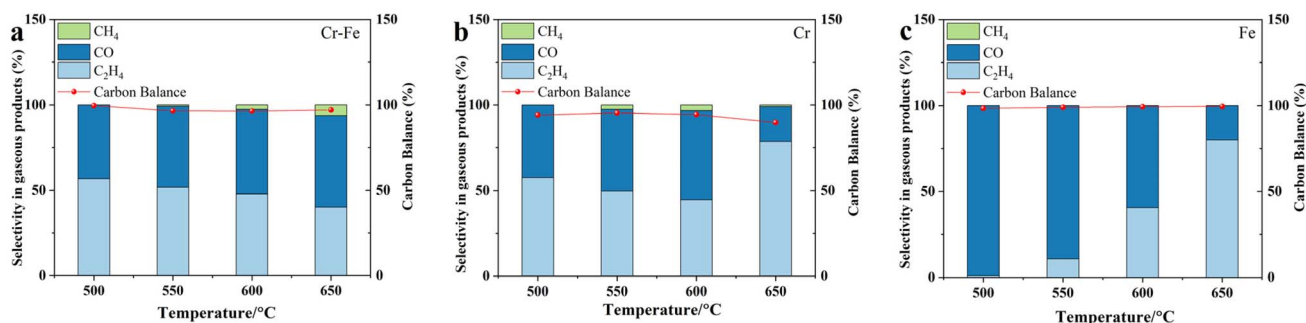


Fig. 2 Selectivity in gaseous products and carbon balance of (a) Cr–Fe, (b) Cr, and (c) Fe.

occurrence of side reactions. Although the ethylene selectivity of the monometallic Cr sample improved at 650 °C, the decline in carbon balance data indicated significant coke formation (Fig. 2b). However, taking the conversion and selectivity into consideration, the highest  $C_2H_4$  yield can be acquired for Cr–Fe samples, reaching nearly 18% at 650 °C (Fig. 1d), which is almost the same as at 700 °C (Fig. S2). This indicates that the Cr–Fe sample exhibits excellent catalytic activity at 600–650 °C, comparable to the ethane conversion and ethylene yields of various Cr-based and Fe-based catalysts reported in the literature (Table S2). In order to exclude the influence of space velocity and inert gas dilution on the inherent activity, the reaction rates normalized by the catalyst weight were calculated. As shown in Table S1, the formation rate of ethylene of the Cr–Fe catalyst was about  $13.4 \mu\text{mol g}_{\text{cat}}^{-1} \text{s}^{-1}$ , which was about 6–7 times higher than that of other reported Fe- and Cr-based catalysts. Considering the low active metal content in supported catalysts, even when normalized to a single active metal, the ethylene formation rate of the Cr–Fe sample remains comparable to others. Furthermore, on the basis of stability tests at 650 °C, a slight decrease in the conversion of  $C_2H_6$  and  $CO_2$  was observed. However, the  $C_2H_4$  yield remained at 18% for 300 min.

### 3.2. Morphological and structural analysis before and after reaction

On the basis of the dramatic difference in catalytic performance between Fe, Cr–Fe, and Cr samples, it is significant to figure out the active site and make clear the “structure–activity” relationship in the  $CO_2$ -ODHE reaction. The powder XRD patterns of the fresh samples are shown in Fig. 3a. The monometallic Fe sample exhibits the hexagonal structure of hematite-type  $Fe_2O_3$  (JCPDS no. 99-0060), according to the diffraction peaks at  $24.2^\circ$ ,  $33.2^\circ$ , and  $35.6^\circ$ . Meanwhile, the peaks at  $24.5^\circ$ ,  $33.6^\circ$ , and  $36.2^\circ$  also demonstrated a typical hexagonal structure of eskolaite-type  $Cr_2O_3$  (JCPDS no. 38-1479) for the monometallic Cr sample. The XRD pattern of the Cr–Fe sample was different from the patterns of  $Fe_2O_3$  and  $Cr_2O_3$ , which can be attributed to mixed oxide  $(Fe,Cr)_2O_3$  (JCPDS no. 35-1112). Taking into consideration that the atomic ratio for Cr to Fe was 3 : 1, the main diffraction peaks (104) and (110) of the fresh Cr–Fe sample were closer to the peak positions of  $Cr_2O_3$ , as shown in Fig. 3b. It

indicated that  $Fe^{3+}$  ions were successfully doped into the  $Cr_2O_3$  lattice to form  $(Fe,Cr)_2O_3$  oxide solid solution in the fresh Cr–Fe sample because of the similar ionic radii of the  $Fe^{3+}$  (0.645 Å) and  $Cr^{3+}$  (0.615 Å) cations.<sup>31</sup> XRD peak broadening is mainly related to the inhomogeneity of the cell size resulting from spatial variations in the amount and distribution of cations and vacancies in  $Cr^{3+}$  and  $Fe^{3+}$ .<sup>32</sup> Consequently, all three samples exhibited the same hexagonal lattice structure. Furthermore, the average particle sizes of all fresh samples were calculated using the Scherrer formula, yielding about 48 nm, 28 nm, and 24 nm for Fe, Cr–Fe, and Cr samples, respectively. It showed that the monometallic Cr sample possesses better anti-sintering ability compared to the monometallic Fe sample, which can also explain the smaller particle size of the fresh Cr–Fe sample due to the formation of a  $(Fe,Cr)_2O_3$  solid solution. Thus, the formation of the  $(Fe,Cr)_2O_3$  solid solution oxide leads to lattice distortion and an increase in lattice defects, inhibiting grain growth and reducing the grain size of Cr–Fe samples. The smaller grain size indicates more exposed active sites, which is beneficial for catalytic reactions.

Taking the high reaction temperature and complex gas atmosphere of the  $CO_2$ -ODHE reaction into consideration, dramatic structural evolution may occur during the reaction. From the XRD patterns of all used samples (Fig. 3c), it is evident that the  $CO_2$ -ODHE reaction induces significant phase transformations in the Fe-containing catalyst samples. For the Fe-used sample, the peaks at  $18.4^\circ$ ,  $30.2^\circ$ , and  $35.3^\circ$  can be attributed to the (111), (220), and (311) planes of cubic phase  $Fe_3O_4$  (JCPDS no. 99-0073). It indicated that  $Fe_2O_3$  was reduced to  $Fe_3O_4$  during  $H_2$  pre-activation and the reaction process. Using the Scherrer formula, the grain size of the monometallic Fe sample was  $\sim 60$  nm after the reaction, suggesting the obvious agglomeration along with the phase transformation during the reaction. For the monometallic Cr sample (initial phase:  $Cr_2O_3$ ), the XRD pattern demonstrated the stability of the  $Cr_2O_3$  phase after the  $H_2$  pre-activation and the reaction process. However, the particle size of  $Cr_2O_3$  increased notably from 24 nm to 36 nm after the reaction. For the Cr–Fe-used sample, there were new diffraction peaks at  $18.3^\circ$ ,  $30.1^\circ$ ,  $35.5^\circ$ ,  $43.1^\circ$ ,  $57.1^\circ$  and  $62.6^\circ$ , indicating the formation of the spinel-structured  $FeCr_2O_4$  component (JCPDS no. 99-0030) with an average particle size of 20.8 nm.<sup>33</sup> Compared with used monometallic Fe and Cr samples, the  $FeCr_2O_4$  component



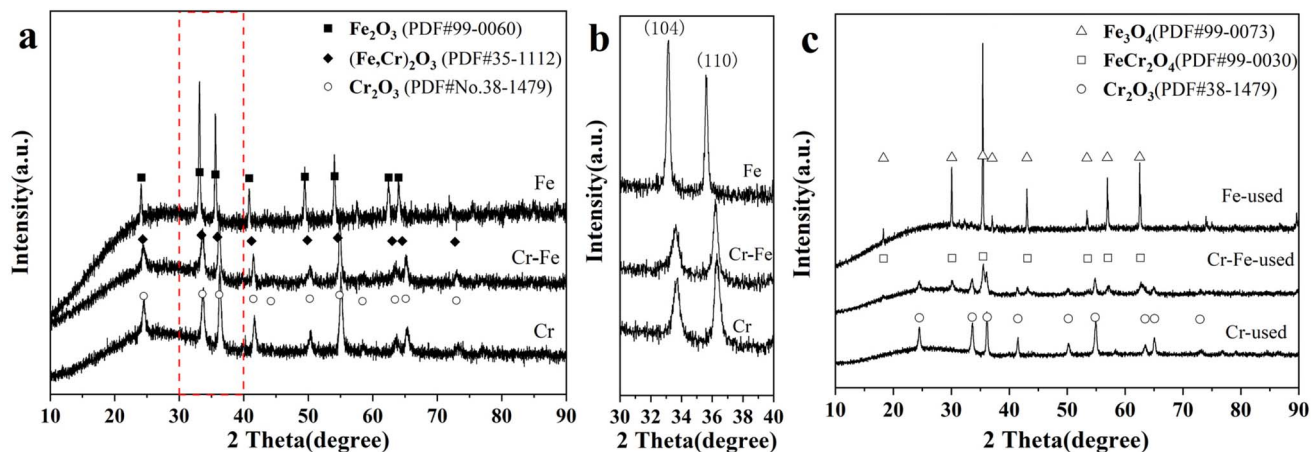


Fig. 3 (a) XRD patterns of fresh  $\text{FeCrO}_x$  catalysts, (b) the magnified portion of the curve in the  $30\text{--}40^\circ$  range in (a), and (c) XRD patterns of used  $\text{FeCrO}_x$  catalysts.

exhibited a better anti-sintering ability. In addition, there was also isolated  $\text{Cr}_2\text{O}_3$  phase in the Cr-Fe-used sample due to the high ratio of Cr/Fe of about 3 : 1. Thus, it can be preliminarily determined that the formation of  $\text{FeCr}_2\text{O}_4$  could improve the catalytic activity of the Cr-Fe sample in the  $\text{CO}_2$ -ODHE reaction. Additionally, the material synthesized with the initial Cr/Fe molar ratio of 2 : 1 was also evaluated to identify the main active phase during the reaction. It was observed that at  $650^\circ\text{C}$ , the ethane conversion (34%),  $\text{CO}_2$  conversion (26%), and ethylene yield (17%) over the 2 : 1 catalyst were largely consistent with those of the 3 : 1 catalyst (Fig. S1). Furthermore, even in the  $\text{Cr}_2\text{Fe}_1$ -used sample, a small amount of  $\text{Cr}_2\text{O}_3$  was detected by XRD (Fig. S3), indicating incomplete consistency with the initial stoichiometric ratio. Nevertheless, the similar catalytic performance in both samples strongly supports that the active species is the spinel-structured  $\text{FeCr}_2\text{O}_4$ , despite the notably lower content of  $\text{Cr}_2\text{O}_3$  in the  $\text{Cr}_2\text{Fe}_1$ -used sample compared to the  $\text{Cr}_3\text{Fe}_1$ -used sample.

In consideration of incomplete dissolution in ICP-OES tests and structural homogeneity for the Cr-Fe sample, the quantitative analysis of iron and chromium elements was performed using XPS fitting results. As shown in Table 1, the surface atomic ratio of Fe to Cr in the Cr-Fe catalyst is 23.1 : 76.9, well consistent with the designed value, verifying the effectiveness of the two-step urea hydrolysis method. Furthermore, the pore

structure and specific surface area of the fresh samples were characterized using  $\text{N}_2$  physical adsorption experiments. The specific surface areas of the fresh Fe, Cr-Fe, and Cr samples are  $13\text{ m}^2\text{ g}^{-1}$ ,  $51\text{ m}^2\text{ g}^{-1}$ , and  $39\text{ m}^2\text{ g}^{-1}$ , respectively. The nitrogen adsorption and desorption isotherms of all catalysts exhibit type V curves, indicating weak interactions between the adsorbent and the adsorbate. The presence of hysteresis loops is caused by the inter-particle pores (Fig. S4). The BJH average pore diameter of the fresh Cr-Fe sample was 20.9 nm, which is significantly smaller than those of the monometallic Fe (44.75 nm) and monometallic Cr (32.13 nm) samples. The particle size of all fresh samples was well consistent with the XRD results. Therefore, the Cr-Fe sample exhibits a higher specific surface area and a smaller particle size than those of the monometallic Fe and Cr samples, which may be beneficial for the adsorption and activation of reactant molecules.

Fig. 4 shows the SEM images of the Fe, Cr-Fe, and Cr catalysts before and after the reaction. It can be seen that the morphology of the three fresh samples was quite similar, all approximately spherical and uniform in size, with secondary particle sizes ranging from several tens to a hundred nanometers, as shown in Fig. 4a(1)–c(1). However, after the  $\text{CO}_2$ -ODHE reaction at  $700^\circ\text{C}$ , there is significant agglomeration and growth in the particle size of the monometallic Fe sample (Fig. 4a(2)), with morphology changing from spherical to

Table 1 Surface atomic ratio, BET surface area, BJH pore size distribution ( $r_p$ ), crystallite size of fresh  $\text{FeCrO}_x$  catalysts and phase composition and crystallite size of used  $\text{FeCrO}_x$  Catalysts

Sample	Surface atomic ratio (Fe/Cr) <sup>a</sup>	$S_{\text{BET}}^b$ ( $\text{m}^2\text{ g}^{-1}$ )	$r_p^b$ (nm)	$D_{\text{fresh}}^c$ (nm)	Phase composition after the reaction	$D_{\text{used}}^d$ (nm)
Fe	100/0	13	44.75	48	$\text{Fe}_3\text{O}_4$	60
Cr-Fe	23.1/76.9	51	20.9	28	$\text{FeCr}_2\text{O}_4/\text{Cr}_2\text{O}_3$	20.8/28.9
Cr	0/100	39	32.13	24	$\text{Cr}_2\text{O}_3$	36.8

<sup>a</sup> Determined by XPS. <sup>b</sup> Calculated from nitrogen adsorption–desorption results. <sup>c</sup> Calculated from the Scherrer formula at the (104) crystal plane of  $(\text{Fe,Cr})_2\text{O}_3$ . <sup>d</sup> Calculated from the Scherrer formula at the related phase in used catalysts.



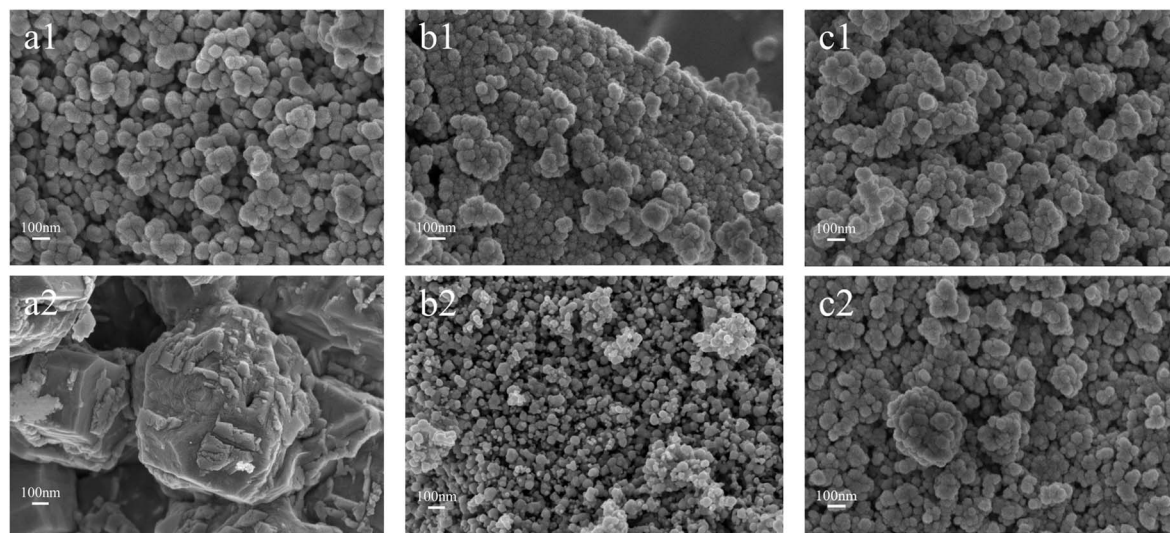


Fig. 4 SEM images of  $\text{FeCrO}_x$  catalyst samples (1) before and (2) after the reaction: (a) Fe, (b) Cr–Fe, and (c) Cr.

angular polygons because of the low melting point of iron oxide and high diffusion rate of iron ions during the transformation of  $\text{Fe}_2\text{O}_3$  into  $\text{Fe}_3\text{O}_4$ .<sup>34,35</sup> In contrast, the spherical morphology of Cr and Cr–Fe samples can be well maintained without obvious aggregation after the  $\text{CO}_2$ -ODHE reaction. It further shows the good anti-sintering ability for the formation of  $\text{FeCr}_2\text{O}_4$ .

Meanwhile, the TEM and HRTEM characterization studies further provided the detailed information about the morphology, size, and shape of the Cr–Fe-used sample under a microdomain view (Fig. 5). The TEM image in Fig. 5a shows that the Cr–Fe-used sample is composed of polyhedron-like nanoparticles with an average particle size of  $\sim 25.5 \pm 8.0$  nm, in good agreement with XRD results. In the high-resolution TEM images, two distinct lattice fringes were clearly visible, in which the interplanar distances of 0.36 nm and 0.48 nm were attributed to the (012) plane of  $\text{Cr}_2\text{O}_3$  and the (111) plane of  $\text{FeCr}_2\text{O}_4$ , respectively. Taking the particle size of the active site over 20 nm, an area of about  $70 \text{ nm}^2$  was chosen to conduct the EDS mapping experiment (Fig. 5c) to ensure data reliability. It indicated that the Cr and Fe elements were distributed uniformly in the component of  $\text{FeCr}_2\text{O}_4$  in some areas, with

isolated Cr element in other areas from  $\text{Cr}_2\text{O}_3$ . It further demonstrated that  $\text{FeCr}_2\text{O}_4$  was stable after the  $\text{CO}_2$ -ODHE reaction.

Fig. 6 presents the Raman spectra for the Fe, Cr, and Cr–Fe samples before and after the reaction to provide fine surface structural information. The Raman spectrum of the fresh Fe sample displayed typical features of  $\text{Fe}_2\text{O}_3$ , with notable peaks at  $224, 245, 292, 407, 496,$  and  $609 \text{ cm}^{-1}$ , corresponding to the six vibrational modes ( $\text{A}_{1g}(1), \text{E}_g(1), \text{E}_g(2), \text{E}_g(3), \text{E}_g(4),$  and  $\text{A}_{1g}(2)$ )<sup>21,36</sup> shown in Fig. 6a. The fresh Cr sample exhibited characteristic Raman peaks of  $\text{Cr}_2\text{O}_3$ , occurring at  $304 \text{ cm}^{-1}$  ( $\text{E}_g$ ),  $341 \text{ cm}^{-1}$  ( $\text{E}_g$ ),  $537 \text{ cm}^{-1}$  ( $\text{A}_g$ ), and  $592 \text{ cm}^{-1}$  ( $\text{E}_g$ )<sup>36–38</sup> (Fig. 6b). For the Cr–Fe mixed sample, the most evident difference in the spectrum of the Cr–Fe mixed oxide compared to its parent binary oxides is the presence of a very strong band in the region of  $560\text{--}700 \text{ cm}^{-1}$ , which is completely absent in the monometallic oxides and is indicative of the characteristic peak of  $\text{FeCrO}_x$  mixed oxide<sup>37,39</sup> (Fig. 6c). Previous studies have indicated that this strong band is associated with magnons, which represent collective excitations of electron spins and anisotropic magnetic interactions within the lattice framework.<sup>36,38,40</sup>

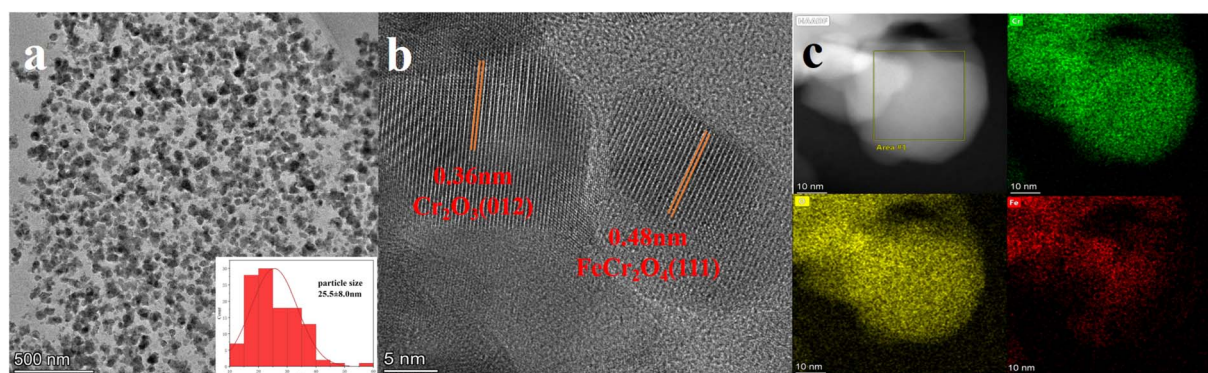


Fig. 5 (a) TEM, (b) high-resolution TEM images and (c) elemental mapping images of the Cr–Fe-used catalyst.





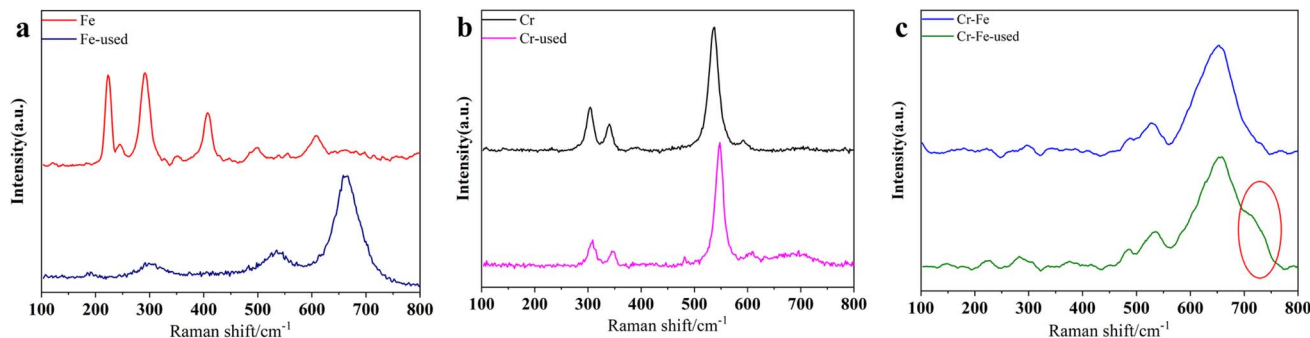


Fig. 6 Raman patterns of (a) Fe, (b) Cr, and (c) Cr-Fe catalysts before and after the reaction.

After the reaction, the Raman spectrum of the Fe-used sample shows significant changes with peaks at 299, 534, and 662  $\text{cm}^{-1}$ , corresponding to  $\text{Fe}_3\text{O}_4$ .<sup>37,39</sup> In contrast, the Cr-used sample shows a blue shift in the characteristic vibrational peaks of  $\text{Cr}_2\text{O}_3$ , indicating the decrease of oxygen vacancies on the catalyst surface after the reaction.<sup>41</sup> Notably, the peak positions of the Cr-Fe-used sample do not show a significant shift after the  $\text{CO}_2$ -ODHE reaction, however, a prominent shoulder

appears at 695–750  $\text{cm}^{-1}$ , confirming the presence of the spinel phase  $\text{FeCr}_2\text{O}_4$  (ref. 21, 37, 39 and 42) in the Cr-Fe-used sample.

The element-sensitive XAFS technique was used to determine the precise electronic and local coordination structures of the Fe and Cr species in used Fe, Cr-Fe, and Cr catalysts. The near-edge region (XANES) of the XAFS spectra provided electronic information about the metal atoms under investigation. The absorption edge energy, white line peak intensity, and pre-

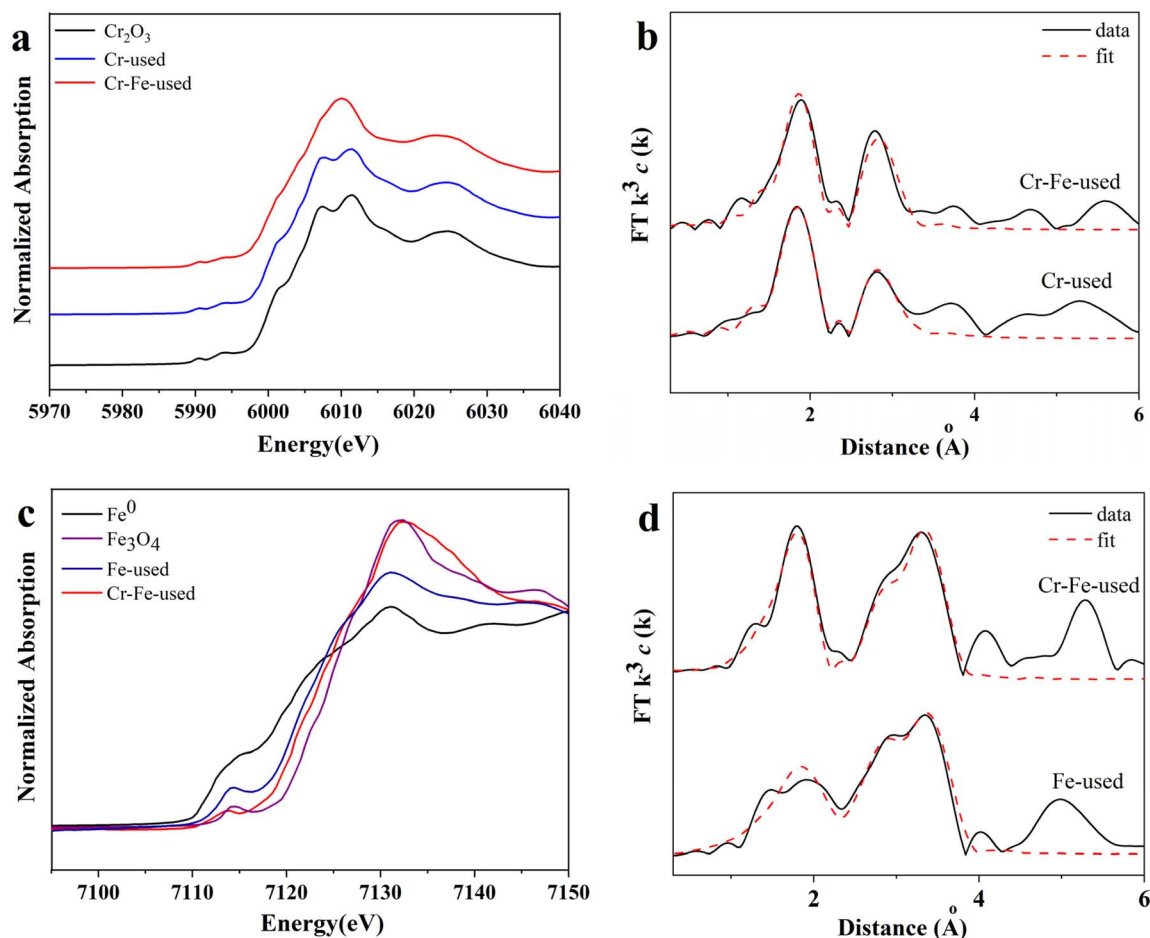


Fig. 7 Cr K-edge: (a) XANES profiles and (b) EXAFS fitting results; Fe K-edge: (c) XANES profiles and (d) EXAFS fitting results in  $R$  space of used  $\text{FeCrO}_x$  catalysts.



edge features are all related to the oxidation state of the metal. The XANES spectra of Cr-used and Cr-Fe-used samples shown in Fig. 7a indicate that the average oxidation state of the Cr element in Cr-containing samples was +3, without further being reduced into the metallic Cr state during the reaction. According to XRD and HRTEM results, the Cr species was involved in the formation of  $\text{Cr}_2\text{O}_3$  and  $\text{FeCr}_2\text{O}_4$  in the Cr-Fe-used sample. There was a strong Cr–O shell at  $\sim 2.0$  Å with a coordination number of  $6.4 \pm 0.7$  and  $6.7 \pm 0.6$  for Cr-used and Cr-Fe-used samples, respectively. For the second shell, a coordination structure of Cr–O–Cr at  $\sim 2.95$  Å can be fitted for Cr-used and Cr-Fe-used samples, in which the coordination number of the Cr–O–Cr/Fe shell for Cr-used ( $\sim 2.5$ ) and Cr-Fe-used ( $\sim 4.5$ ) samples was obviously different (Fig. 7b and Table S3). It further demonstrated that  $\text{FeCr}_2\text{O}_4$  possessed a different coordination structure with  $\text{Cr}_2\text{O}_3$ .

Furthermore, the Fe K-edge (7112 eV) XAFS measurements of the Fe-used and Cr-Fe-used catalysts were also conducted as shown in Fig. 7c and d and Table S4. The edge jump energies of the Fe-used and Cr-Fe-used catalysts were between those of Fe-foil and  $\text{Fe}_3\text{O}_4$ . The average oxidation state of iron for the Fe-used and Cr-Fe-used catalysts was +2.2 and +2.6, respectively, calculated from linear combination fitting results shown in Fig. S5 and Table S4. The EXAFS spectra of the Fe-used and Cr-Fe-used samples shown in Fig. 7d exhibited the coordination structure of Fe species. For the Fe-used sample, the Fe–O ( $R \approx 2.0$  Å, CN  $\approx 3.9$ ), Fe–O–Fe1 ( $R \approx 2.97$  Å, CN  $\approx 3.9$ ) and Fe–O–Fe2 ( $R \approx 3.49$  Å, CN  $\approx 11.6$ ) shells were acquired, which were assigned to the typical  $\text{Fe}_3\text{O}_4$  structure. In addition, a tiny metallic Fe–Fe ( $R \approx 2.52$  Å, CN  $\approx 1.2$ ) shell was necessary for the fitting data of Fe-used sample, which was well consistent with the lower average oxidation state over iron species. For the Cr-Fe-used sample, the coordination number of the Fe–O shell at  $R \approx 1.94$  Å increased to 5.4. Moreover, there were Fe–O–Fe1 ( $R \approx 2.92$  Å, CN  $\approx 2.4$ ) and Fe–O–Cr ( $R \approx 3.47$  Å, CN  $\approx 12.1$ ) shells for the fitting results. According to XAFS results, it can be seen that there were more oxygen atoms surrounding Fe species in  $\text{FeCr}_2\text{O}_4$ , which may be beneficial for the elimination of deposited coke. Based on the combined results of XRD, HRTEM and XAFS results, we can confirm that the main active sites in Fe, Cr-Fe and Cr samples are  $\text{Fe}_3\text{O}_4$ ,  $\text{FeCr}_2\text{O}_4$  and  $\text{Cr}_2\text{O}_3$ , respectively.

Additionally, the phase transformation process of the Cr-Fe catalyst from hydrogenation pretreatment to the  $\text{CO}_2$ -ODHE reaction was *in situ* monitored by synchrotron radiation XRD (SR-XRD). The 2D-XRD pattern exhibits distinct concentric rings, with a non-uniform intensity distribution of the diffraction rings observed within the azimuthal angle range of  $0^\circ$ – $180^\circ$ , indicating a preferred orientation of the crystals along specific crystal planes (Fig. 8). Through radial integration, the 2D image was converted into a 1D diffraction pattern. As expected, the fresh sample exhibited clearly visible diffraction rings, ordered from the center outward, corresponding to the diffraction peaks at  $24.3$ ,  $33.5$ ,  $35.9$ ,  $41.2$ ,  $49.8$ , and  $54.6^\circ$ , which are indexed to the (012), (104), (110), (113), (024), and (116) crystal planes of the  $(\text{Fe,Cr})_2\text{O}_3$  (JCPDS no. 35-1112) solid solution at room temperature (Fig. 8a and b), respectively. After the

reduction, the  $(\text{Fe,Cr})_2\text{O}_3$  solid solution was gradually reduced to  $\text{Fe}^0$  (JCPDS no. 06-0696) with the appearance of an additional diffraction ring at  $44.5^\circ$  (indicated by an arrow in Fig. 8c). The diffraction peaks at  $24.5$ ,  $33.6$ , and  $36.2^\circ$  of  $\text{Cr}_2\text{O}_3$  (JCPDS no. 38-1479) became distinctly visible. Upon switching to the reaction atmosphere, the disappearance of the  $\text{Fe}^0$  diffraction peak at  $44.5^\circ$  indicates that  $\text{Fe}^0$  cannot remain stable under the reaction conditions in the presence of the oxidizing  $\text{CO}_2$  atmosphere. The absence of diffraction peaks at  $33.4$ ,  $41.2$ , and  $49.8^\circ$  signified the complete disappearance of the  $(\text{Fe,Cr})_2\text{O}_3$  solid solution phase, and the new diffraction peaks at  $30.1$ ,  $35.5$ , and  $57.1^\circ$  just appeared, corresponding to the diffraction ring observed at the position indicated by the arrow in Fig. 8d, indicating the formation of  $\text{FeCr}_2\text{O}_4$  under the reaction conditions. Furthermore, with the progress of reaction, the  $\text{FeCr}_2\text{O}_4$  component was generated and maintained for the whole reaction.

Moreover, when the pretreatment gas was altered to air and inert gas (Ar) instead of the reducing hydrogen atmosphere (Fig. S6), it was observed that a reducing pretreatment atmosphere slightly favored the conversion of ethane compared to the others at lower temperatures, suggesting that the reductive pretreatment atmosphere promotes the phase transformation process, thereby effectively shortening the induction period for the generation of the active phase. Notably, even when oxidative (air) or inert (Ar) atmospheres are used instead of  $\text{H}_2$  pretreatment, the  $\text{FeCr}_2\text{O}_4$  phase remains stable after the reaction (Fig. S7), which may be due to the inevitable generation of reductive  $\text{H}_2$  in the  $\text{CO}_2$ -ODHE reaction. Therefore, the *in situ* XRD experiments further confirmed the generation of spinel-structured  $\text{FeCr}_2\text{O}_4$  during the  $\text{CO}_2$ -ODHE reaction, which had previously been identified as the active phase for this reaction through TEM and Raman characterization.

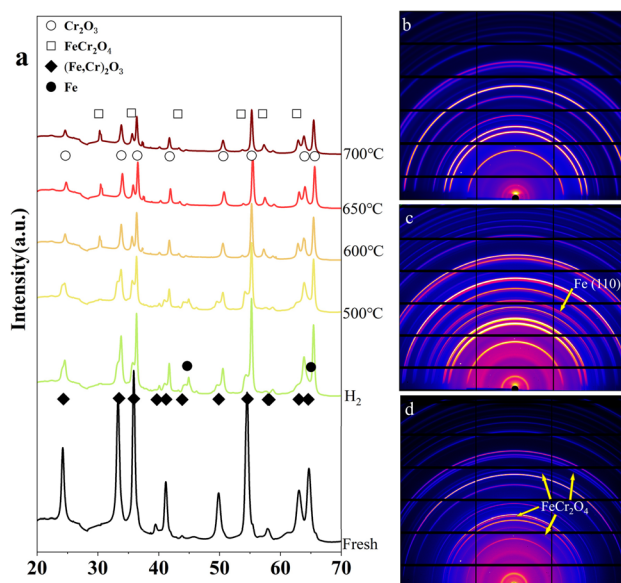


Fig. 8 *In situ* SR-XRD (a) patterns of the Cr-Fe catalyst during the  $\text{CO}_2$ -ODHE reaction and 2D images of (b) fresh catalyst (c) after pretreatment at  $450^\circ\text{C}$  in  $50\% \text{H}_2/\text{Ar}$  and (d) at  $650^\circ\text{C}$  in the reaction gases ( $\text{CO}_2/\text{C}_2\text{H}_6/\text{Ar} = 10/10/20 \text{ mL min}^{-1}$ ).



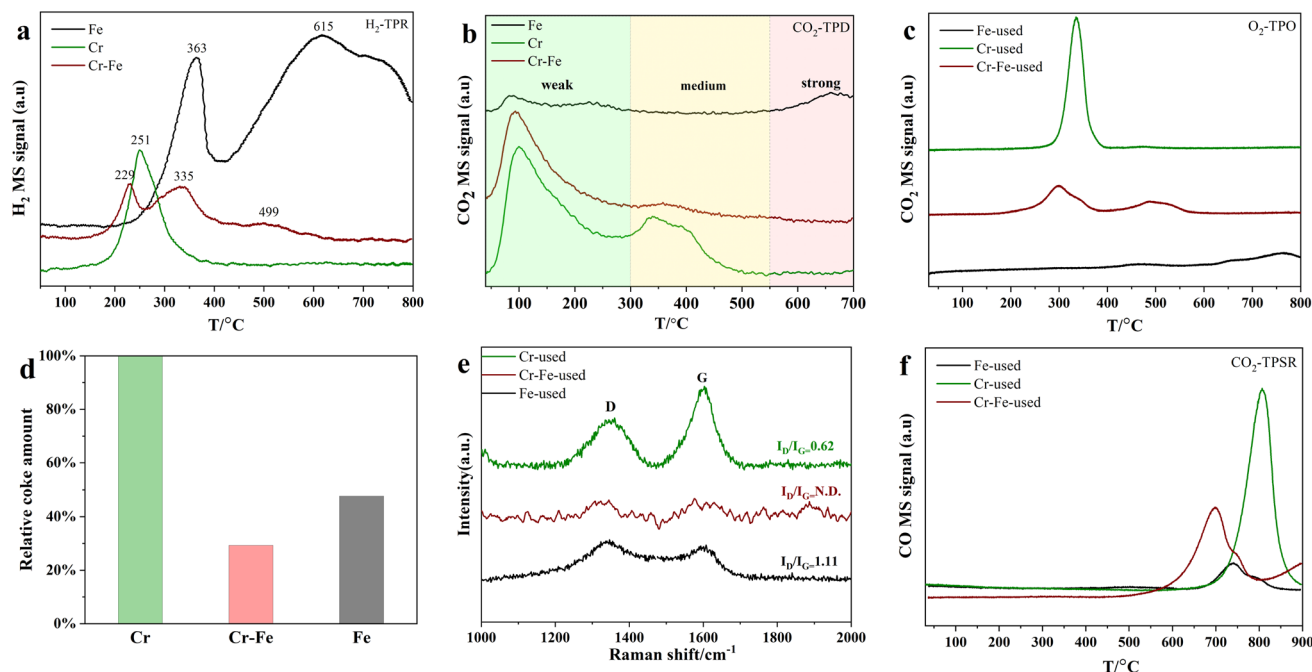


Fig. 9 (a)  $\text{H}_2$ -TPR of fresh  $\text{FeCrO}_x$  samples, (b)  $\text{CO}_2$ -TPD of  $\text{FeCrO}_x$  samples, (c)  $\text{O}_2$ -TPO and (f)  $\text{CO}_2$ -TPSR of the used  $\text{FeCrO}_x$  samples, (d) the estimated relative coke deposition on the catalyst from (c), and (e) Raman spectra of used  $\text{FeCrO}_x$  samples in the wavenumber range of 1000–2000  $\text{cm}^{-1}$ .

### 3.3. Catalyst reaction mechanism

To further investigate the reducibility and metal-oxide interaction of the  $\text{FeCrO}_x$  catalysts,  $\text{H}_2$ -TPR characterization was conducted on the Fe, Cr, and Cr-Fe samples. As shown in Fig. 9a, the fresh Fe sample exhibits two peaks at 363 °C and after 400 °C (with a peak centered at 615 °C). The first peak was assigned to the reduction of  $\text{Fe}_2\text{O}_3$  to  $\text{Fe}_3\text{O}_4$ , while the latter peak (after 400 °C) can be attributed to the reduction of  $\text{Fe}_3\text{O}_4$  to  $\text{Fe}^{2+}$  and  $\text{Fe}^0$ .<sup>43–45</sup> For the fresh Cr sample, only a reduction peak at 251 °C can be observed, originating from the reduction of surface  $\text{Cr}^{6+}$  species to  $\text{Cr}^{3+}$ , which are reported to coexist on the catalyst surface under oxidizing conditions<sup>12,14</sup> and are reduced at relatively low temperatures (200–300 °C).<sup>21,35,46</sup> For the fresh Cr-Fe samples, the reduction peaks at 229, 335 and 499 °C were attributed to the reduction of surface  $\text{Cr}^{6+}$  species,  $\text{Fe}^{3+}$  to  $\text{Fe}^{2+}$  and  $\text{Fe}^0$ , which were much lower than those in monometallic Fe and Cr samples. It indicated that the formation of the  $(\text{Fe,Cr})_2\text{O}_3$  solid solution can improve the reducibility of Fe and Cr species.

We used  $\text{CO}_2$ -TPD experiments to characterize the  $\text{CO}_2$  adsorption capacity of active site properties for different

catalysts. The basicity of catalysts, which can be correlated with their  $\text{CO}_2$  desorption temperature, is typically categorized as follows: weak (<300 °C), medium (300–500 °C) and strong (>500 °C). Prior to TPD, the catalyst sample was processed with 5%  $\text{H}_2/\text{Ar}$  (50  $\text{mL min}^{-1}$ ) at 450 °C for 90 min. As shown in Fig. 9b and Table 2, the Fe sample exhibits tiny  $\text{CO}_2$  desorption peaks at 90 °C and 660 °C, indicating the weak  $\text{CO}_2$  adsorption capacity of  $\text{Fe}_3\text{O}_4$ . It was also in agreement with the catalytic performance, in which the Fe catalyst exhibited low  $\text{CO}_2$  conversion. For the Cr catalyst, the  $\text{CO}_2$  desorption peaks occurred primarily at 100 °C and 338 °C, which are assigned to weak and medium basic sites, respectively. This demonstrates that  $\text{Cr}_2\text{O}_3$  is beneficial for adsorbing  $\text{CO}_2$  to participate in the  $\text{CO}_2$ -ODHE reaction, thereby contributing to the higher  $\text{CO}_2$  conversion over the Cr catalyst (Fig. 1b). However, for the Cr-Fe sample, only a visual and strong  $\text{CO}_2$  adsorption peak at ~100 °C can be detected, suggesting weak basicity on  $\text{FeCr}_2\text{O}_4$ , in which the weak basicity may be a key factor in the higher  $\text{C}_2\text{H}_4$  yield for the Cr-Fe sample. The presence of weak basic sites improved selectivity to alkene and reduced coke formation.<sup>47</sup> In contrast, the strong basic sites favor the side reactions, such as reforming and cracking reactions, leading to significant coke deposition and reduced reaction activity.<sup>14</sup> The He-TPSR experiments confirmed that both the  $\text{Cr}_2\text{O}_3$  and  $\text{FeCr}_2\text{O}_4$  catalysts contain certain active oxygen species capable of reacting with deposited coke, exhibiting similar light-off temperatures (Fig. S8). However,  $\text{CO}_2$  molecules adsorbed on the weak and medium basic sites should be relatively active and can readily participate in reactions, especially the weak basic sites.<sup>48</sup> Therefore, the Cr-Fe sample exhibits superior  $\text{CO}_2$  adsorption

Table 2  $\text{CO}_2$  desorption peak area for  $\text{FeCrO}_x$  catalysts<sup>a</sup>

Sample	$S_{\text{weak}}/S_{\text{medium}}/S_{\text{strong}} (\times 10^{-7})$
Fe	2.6/0/0.6
Cr-Fe	12.5/0.3/0
Cr	18.5/3.2/0

<sup>a</sup> Estimated by  $\text{CO}_2$ -TPD.





and activation capabilities, attributable to its weak basic sites. This property facilitates the gasification of carbon deposits, thereby effectively mitigating coke accumulation. Furthermore, the O<sub>2</sub>-TPO experiment also certified the lowest amount of coke deposition in the Cr-Fe-used sample (Fig. 9c). Generally, the carbon species with a lower peak temperature shows a higher activity and can be easily removed.<sup>18,49</sup> For the Cr-used sample, a strong CO<sub>2</sub> peak at 330 °C can be observed, which was well consistent with the low carbon balance shown in Fig. 2b. Furthermore, two peaks at ~300 °C and 500 °C were acquired in the Cr-Fe-used sample, which can be attributed to the oxidation of coke on Cr<sub>2</sub>O<sub>3</sub> and FeCr<sub>2</sub>O<sub>4</sub> respectively, with much less coke deposition on FeCr<sub>2</sub>O<sub>4</sub>. For Fe-used samples, the amount of coke deposited is small because of low activity in the CO<sub>2</sub>-ODHE reaction. By integrating the CO<sub>2</sub> peaks from the mass spectrometry data and normalizing against the ethane conversion rate, we compared the relative coke amounts per unit mass of used catalysts (Fig. 9d). The monometallic Cr-used sample exhibited the highest quantity of coke deposition, despite its lower activity compared to the Cr-Fe-used catalysts, due to its medium basicity. The Raman spectra of used samples (Fig. 9e) also showed that the Fe-used and Cr-used samples exhibited prominent D bands (disorder-induced, ~1430 cm<sup>-1</sup>) and G bands (in-plane vibrations, ~1610 cm<sup>-1</sup>) associated with coke deposition.<sup>50</sup> However, these tiny peaks at ~1430 cm<sup>-1</sup> and ~1610 cm<sup>-1</sup> in the Cr-Fe-used sample made it impossible to evaluate the degree of carbon graphitization using the I<sub>D</sub>/I<sub>G</sub> intensity ratio value. In addition, the conversion of CO<sub>2</sub> plays a key role in the elimination of coke deposition in the CO<sub>2</sub>-ODHE reaction through the oxidation of coke by the CO<sub>2</sub> molecule. In Fig. 9f, it can be seen that CO<sub>2</sub> can react with surface deposited coke to release CO at 550 °C in the Cr-Fe-used sample, continuing up to 800 °C. The results indicate that FeCr<sub>2</sub>O<sub>4</sub> can effectively activate CO<sub>2</sub> molecules, enabling the Boudouard reaction (C + CO<sub>2</sub> → 2CO) with deposited coke even at relatively low temperatures. Moreover, CO<sub>2</sub> in the reaction stream continuously reacts with carbon deposits across the entire temperature range of the CO<sub>2</sub>-ODHE reaction (500–700 °C), thereby contributing to the improvement of catalytic performance. In contrast, significant CO release for the monometallic catalyst samples was observed only at 700 °C. Despite the continuous oxygen supply from CO<sub>2</sub> before this temperature, it could not react with the surface coke on the catalysts, aligning with the observed reaction activity. Based on these results, it can be concluded that the FeCr<sub>2</sub>O<sub>4</sub> phase effectively adsorbs and activates CO<sub>2</sub>, thereby facilitating coke removal and promoting the CO<sub>2</sub>-ODHE reaction.

Additionally, the Cr-Fe sample that lost activity after the stability test (650 °C, >12 h) was regenerated by calcining in air at 600 °C to remove coke (Fig. S9a). Subsequent stability tests showed that the initial conversion rates and yields were restored but revealed recurring deactivation patterns with continued reaction, indicating that the gradual accumulation of coke is the primary cause of FeCrO<sub>x</sub> catalyst deactivation. Significantly, CO<sub>2</sub>-TPSR results demonstrate the ability of FeCr<sub>2</sub>O<sub>4</sub> to activate CO<sub>2</sub> for low-temperature carbon gasification. To validate this *in situ* regeneration strategy, we performed cyclic CO<sub>2</sub> treatments

on deactivated catalysts (Fig. S9b). Each regeneration cycle substantially restored ethane conversion (>95% recovery) while maintaining ethylene yield above 15% throughout repeated testing. These findings collectively establish continuous CO<sub>2</sub> purging as a promising operational strategy to mitigate coke-induced deactivation during the reaction.

## 4. Conclusions

In summary, nano-iron oxide, chromium oxide, and FeCr bimetallic oxides were synthesized using a two-step urea precipitation method and subjected to CO<sub>2</sub> oxidative dehydrogenation of ethane catalytic tests. The Cr-Fe sample exhibited significantly higher activity compared to the monometallic samples with the conversion of ethane and CO<sub>2</sub> approaching 35% and 27% at 650 °C, respectively. And the formation rate of C<sub>2</sub>H<sub>4</sub> was about 13.4 μmol g<sub>cat</sub><sup>-1</sup> s<sup>-1</sup> with the C<sub>2</sub>H<sub>4</sub> yield remaining at 18% for 300 min. Through XRD, Raman, SEM and XAFS characterization, it was found that the monometallic Fe sample transformed from Fe<sub>2</sub>O<sub>3</sub> to Fe<sub>3</sub>O<sub>4</sub> during the reaction and underwent sintering. Although the monometallic Cr sample did not show significant phase changes, it tends to deactivate due to substantial coke formation. In contrast, the bimetallic Cr-Fe sample formed a solid solution oxide of (Fe,Cr)<sub>2</sub>O<sub>3</sub>, effectively reducing the catalyst grain size and resisting sintering. The *in situ* formation and stable spinel structure of FeCr<sub>2</sub>O<sub>4</sub> during the reaction, which were characterized by synchrotron radiation-based *in situ* XRD, confirm that FeCr<sub>2</sub>O<sub>4</sub> is the active phase for the CO<sub>2</sub>-ODHE reaction. Moreover, the Cr-Fe sample with weak basic sites exhibits superior CO<sub>2</sub> adsorption and activation capabilities. According to O<sub>2</sub>-TPO and CO<sub>2</sub>-TPSR of the used samples, FeCr<sub>2</sub>O<sub>4</sub> enables the combustion of coke deposited on the catalyst surface at lower temperatures, thus significantly enhancing the reaction activity and regeneration stability. Our work may provide theoretical guidance for the industrial application of non-noble metal catalysts in CO<sub>2</sub> oxidative dehydrogenation of ethane.

## Conflicts of interest

There are no conflicts to declare.

## Data availability

The authors confirm that the data supporting the findings of this study are available within the article and its SI. See DOI: <https://doi.org/10.1039/d5ta05111h>.

## Acknowledgements

This work was supported by the “Photon Science Research Center for Carbon Dioxide”, “Project of the National Natural Science Foundation of China” (22332003 and 12505386), Science and Technology Innovation Plan of Shanghai Science and Technology Commission (23YF1453700), “Shanghai Municipal Science and Technology Commission” (23JC1403300), “2025 Research Equipment Project of the



Special Fund for Improving Research Conditions in Central-Level Scientific Institutions, Chinese Academy of Sciences” and “Shanghai Municipal Science and Technology Major Project”. We appreciate the assistance of TILON Group Technology Limited (Division of China) in characterization of catalysts. Additionally, the User Experiment Assist System (<https://cstr.cn/31124.02.SSRF.LAB>), 14W1, 02U2, 13SSW, 17B, and 16U1 beamline of SSRF provided support for data collection for this work.

## References

- 1 J. F. S. de Oliveira, D. P. Volanti, J. M. C. Bueno and A. P. Ferreira, Effect of CO<sub>2</sub> in the oxidative dehydrogenation reaction of propane over Cr/ZrO<sub>2</sub> catalysts, *Appl. Catal., A*, 2018, **558**, 55–66, DOI: [10.1016/j.apcata.2018.03.020](https://doi.org/10.1016/j.apcata.2018.03.020).
- 2 G.-Q. Yang, H. Wang, T. Gong, Y.-H. Song, H. Feng, H.-Q. Ge, H.-b. Ge, Z.-T. Liu and Z.-W. Liu, Understanding the active-site nature of vanadia-based catalysts for oxidative dehydrogenation of ethylbenzene with CO<sub>2</sub> via atomic layer deposited VO<sub>x</sub> on  $\gamma$ -Al<sub>2</sub>O<sub>3</sub>, *J. Catal.*, 2019, **380**, 195–203, DOI: [10.1016/j.jcat.2019.10.009](https://doi.org/10.1016/j.jcat.2019.10.009).
- 3 L.-C. Wang, Y. Zhang, J. Xu, W. Diao, S. Karakalos, B. Liu, X. Song, W. Wu, T. He and D. Ding, Non-oxidative dehydrogenation of ethane to ethylene over ZSM-5 zeolite supported iron catalysts, *Appl. Catal., B*, 2019, **256**, 117816, DOI: [10.1016/j.apcatb.2019.117816](https://doi.org/10.1016/j.apcatb.2019.117816).
- 4 Y. Zhang, M. Chen, W. Wang and Y. Zhang, A stable Pt modified cobalt tungstate catalyst for CO<sub>2</sub>-assisted oxidative dehydrogenation of ethane, *Catal. Sci. Technol.*, 2024, **14**(14), 3924–3935, DOI: [10.1039/d4cy00399c](https://doi.org/10.1039/d4cy00399c).
- 5 E. Gomez, B. Yan, S. Kattel and J. G. Chen, Carbon dioxide reduction in tandem with light-alkane dehydrogenation, *Nat. Rev. Chem.*, 2019, **3**(11), 638–649, DOI: [10.1038/s41570-019-0128-9](https://doi.org/10.1038/s41570-019-0128-9).
- 6 P. Liu, L. Zhang, M. Li, N. Sun and W. Wei, Recent progress in Cr-based catalysts for oxidative dehydrogenation of light alkanes by employing CO<sub>2</sub> as a soft oxidant, *Clean Energy*, 2021, **5**(4), 623–633, DOI: [10.1093/ce/ckab036](https://doi.org/10.1093/ce/ckab036).
- 7 T. A. Bugrova, V. V. Dutov, V. A. Svetlichnyi, V. Cortés Corberán and G. V. Mamontov, Oxidative dehydrogenation of ethane with CO<sub>2</sub> over CrO<sub>x</sub> catalysts supported on Al<sub>2</sub>O<sub>3</sub>, ZrO<sub>2</sub>, CeO<sub>2</sub> and Ce<sub>x</sub>Zr<sub>1-x</sub>O<sub>2</sub>, *Catal. Today*, 2019, **333**, 71–80, DOI: [10.1016/j.cattod.2018.04.047](https://doi.org/10.1016/j.cattod.2018.04.047).
- 8 Y. Gambo, S. Adamu, G. Tanimu, I. M. Abdullahi, R. A. Lucky, M. S. Ba-Shammakh and M. M. Hossain, CO<sub>2</sub>-mediated oxidative dehydrogenation of light alkanes to olefins: advances and perspectives in catalyst design and process improvement, *Appl. Catal., A*, 2021, **623**, 118273, DOI: [10.1016/j.apcata.2021.118273](https://doi.org/10.1016/j.apcata.2021.118273).
- 9 M. Maroño, E. Ruiz, J. M. Sánchez, C. Martos, J. Dufour and A. Ruiz, Performance of Fe–Cr based WGS catalysts prepared by co-precipitation and oxi-precipitation methods, *Int. J. Hydrogen Energy*, 2009, **34**(21), 8921–8928, DOI: [10.1016/j.ijhydene.2009.08.068](https://doi.org/10.1016/j.ijhydene.2009.08.068).
- 10 M. D. Porosoff, M. N. Z. Myint, S. Kattel, Z. Xie, E. Gomez, P. Liu and J. G. Chen, Identifying Different Types of Catalysts for CO<sub>2</sub> Reduction by Ethane through Dry Reforming and Oxidative Dehydrogenation, *Angew. Chem., Int. Ed.*, 2015, **54**(51), 15501–15505, DOI: [10.1002/anie.201508128](https://doi.org/10.1002/anie.201508128).
- 11 Y. Cheng, H. Gong, C. Miao, W. Hua, Y. Yue and Z. Gao, Ga<sub>2</sub>O<sub>3</sub>/HSSZ-13 for dehydrogenation of ethane: effect of pore geometry of support, *Catal. Commun.*, 2015, **71**, 42–45, DOI: [10.1016/j.catcom.2015.08.015](https://doi.org/10.1016/j.catcom.2015.08.015).
- 12 S. Wang, K. Murata, T. Hayakawa, S. Hamakawa and K. Suzuki, Dehydrogenation of ethane with carbon dioxide oversupported chromium oxide catalysts, *Appl. Catal., A*, 2000, **196**, 1–8.
- 13 R. Koirala, O. V. Safonova, S. E. Pratsinis and A. Baiker, Effect of cobalt loading on structure and catalytic behavior of CoO<sub>x</sub>/SiO<sub>2</sub> in CO<sub>2</sub>-assisted dehydrogenation of ethane, *Appl. Catal., A*, 2018, **552**, 77–85, DOI: [10.1016/j.apcata.2017.12.025](https://doi.org/10.1016/j.apcata.2017.12.025).
- 14 S. Deng, H. Li, S. Li and Y. Zhang, Activity and characterization of modified Cr<sub>2</sub>O<sub>3</sub>/ZrO<sub>2</sub> nano-composite catalysts for oxidative dehydrogenation of ethane to ethylene with CO<sub>2</sub>, *J. Mol. Catal. A: Chem.*, 2007, **268**(1–2), 169–175, DOI: [10.1016/j.molcata.2006.12.033](https://doi.org/10.1016/j.molcata.2006.12.033).
- 15 M. Numan, E. Eom, A. Li, M. Mazur, H. W. Cha, H. C. Ham, C. Jo and S.-E. Park, Oxidative Dehydrogenation of Ethane with CO<sub>2</sub> as a Soft Oxidant over a PtCe Bimetallic Catalyst, *ACS Catal.*, 2021, **11**(15), 9221–9232, DOI: [10.1021/acscatal.1c01156](https://doi.org/10.1021/acscatal.1c01156).
- 16 N. Mimura, I. Takahara, M. Inaba, M. Okamoto and K. Murata, High-performance Cr/H-ZSM-5 catalysts for oxidative dehydrogenation of ethane to ethylene with CO<sub>2</sub> as an oxidant, *Catal. Commun.*, 2002, **3**(6), 257–262, DOI: [10.1016/s1566-7367\(02\)00117-6](https://doi.org/10.1016/s1566-7367(02)00117-6).
- 17 M. Numan, T. Kim, C. Jo and S.-E. Park, Ethane Dehydrogenation with CO<sub>2</sub> as a soft oxidant over a Cr-TUD-1 catalyst, *J. CO<sub>2</sub> Util.*, 2020, **39**, 101184, DOI: [10.1016/j.jcou.2020.101184](https://doi.org/10.1016/j.jcou.2020.101184).
- 18 B. Yan, S. Yao, S. Kattel, Q. Wu, Z. Xie, E. Gomez, P. Liu, D. Su and J. G. Chen, Active sites for tandem reactions of CO<sub>2</sub> reduction and ethane dehydrogenation, *Proc. Natl. Acad. Sci. U. S. A.*, 2018, **115**(33), 8278–8283, DOI: [10.1073/pnas.1806950115](https://doi.org/10.1073/pnas.1806950115).
- 19 S. Deng, S.-G. Li, H.-Q. Li and Y. Zhang, Oxidative dehydrogenation of ethane to ethylene with CO<sub>2</sub> over Fe-CrZrO<sub>2</sub> catalysts, *Ind. Eng. Chem. Res.*, 2009, **48**, 7561–7566, DOI: [10.1021/ie9007387](https://doi.org/10.1021/ie9007387).
- 20 V. Kocovski, G. Pilania and B. P. Uberuaga, High-throughput investigation of the formation of double spinels, *J. Mater. Chem. A*, 2020, **8**(48), 25756–25767, DOI: [10.1039/d0ta09200b](https://doi.org/10.1039/d0ta09200b).
- 21 S. Bhandari, R. Khatun, T. S. Khan, D. Khurana, M. K. Poddar, A. Shukla, V. V. D. N. Prasad and R. Bal, Preparation of a nanostructured iron chromite spinel in the pure form and its catalytic activity for the selective oxidation of benzene to phenol: experimental and DFT



- studies, *Green Chem.*, 2022, **24**(23), 9303–9314, DOI: [10.1039/d2gc02335k](#).
- 22 I. I. Mishanin and V. I. Bogdan, *In situ* CO<sub>2</sub> reactivation of FeCrO/C catalyst in the oxidative dehydrogenation of ethane to ethylene, *Mendeleev Commun.*, 2020, **30**(3), 359–361, DOI: [10.1016/j.mencom.2020.05.033](#).
  - 23 I. I. Mishanin, T. V. Bogdan, A. E. Koklin and V. I. Bogdan, Design of highly selective heterogeneous catalyst for CO<sub>2</sub>-mediated ethane oxidative dehydrogenation based on nonoxidative catalysis in stainless-steel reactor, *Chem. Eng. J.*, 2022, **446**, 137184, DOI: [10.1016/j.cej.2022.137184](#).
  - 24 I. I. Mishanin, T. V. Bogdan, A. V. Smirnov, P. A. Chernavskii, N. N. Kuznetsova and V. I. Bogdan, Formation of active phases of Fe/C, Cr/C and Fe–Cr/C catalysts in oxidative dehydrogenation of ethane, *Mendeleev Commun.*, 2023, **33**(3), 422–424, DOI: [10.1016/j.mencom.2023.04.039](#).
  - 25 O. A. Kim, T. V. Bogdan, A. E. Koklin and V. I. Bogdan, Interaction of Carbon Dioxide with Hydrogen on Supported Fe, Cr-Containing Catalysts, *Russ. J. Phys. Chem. B*, 2023, **16**(7), 1218–1220, DOI: [10.1134/s1990793122070107](#).
  - 26 T. V. Bogdan, A. E. Koklin, I. I. Mishanin, P. A. Chernavsky, D. A. Pankratov, O.-S. A. Kim and V. Bogdan, CO<sub>2</sub> Hydrogenation on Carbides Formed *in situ* on Carbon-Supported Iron-Based Catalysts in High-Density Supercritical Medium, *ChemPlusChem*, 2024, **89**, e202400327, DOI: [10.1002/cplu.202400327](#).
  - 27 B. Ravel and M. Newville, ATHENA, ARTEMIS, HEPHAESTUS: data analysis for X-ray absorption spectroscopy using IFEFFIT, *J. Synchrotron Radiat.*, 2005, **12**(4), 537–541, DOI: [10.1107/s0909049505012719](#).
  - 28 F. Cancino-Trejo, V. Santes, J. A. A. Cardenas, M. Gallardo, Y. G. Maldonado, L. Miranda A, O. Valdes, J. A. de los Reyes and C. E. Santolalla-Vargas, Active Ni and Fe species on catalysts Ni/Al<sub>2</sub>O<sub>3</sub> and NiFe/Al<sub>2</sub>O<sub>3</sub> for the oxidative dehydrogenation (ODH) of ethane to ethylene assisted by CO<sub>2</sub>, *Chem. Eng. J. Adv.*, 2022, **12**, 100404, DOI: [10.1016/j.cej.2022.100404](#).
  - 29 P. Liu, L. Zhang, X. Wang, M. Du, Y. Hao, L. Li, X. Chen, N. Sun and W. Wei, Preparation, Structure-Performance Relationship, and Reaction Network of ZnZSM-5 for Oxidative Dehydrogenation of Ethane with CO<sub>2</sub>, *Chemistry*, 2023, **29**(22), e202203960, DOI: [10.1002/chem.202203960](#).
  - 30 S. Yao, B. Yan, Z. Jiang, Z. Liu, Q. Wu, J. H. Lee and J. G. Chen, Combining CO<sub>2</sub> Reduction with Ethane Oxidative Dehydrogenation by Oxygen-Modification of Molybdenum Carbide, *ACS Catal.*, 2018, **8**(6), 5374–5381, DOI: [10.1021/acscatal.8b00541](#).
  - 31 R. D. Shannon, Revised effective ionic radii and systematic studies of interatomic distances in halides and chalcogenides, *Acta Crystallogr., Sect. A*, 1976, **32**, 751–767, DOI: [10.1107/s0567739476001551](#).
  - 32 M. E. Montero-Cabrera, L. E. Fuentes-Cobas, E. Macías-Ríos and M. E. Fuentes-Montero, Application of X-ray absorption fine structure (XAFS) to local-order analysis in Fe–Cr maghemite-like materials, *AIP Conf. Proc.*, 2015, **1671**, 020008, DOI: [10.1063/1.4927185](#).
  - 33 M. García-Vázquez, K. Wang, J. M. González-Carballo, D. Brown, P. Landon, R. Tooze and F. R. García-García, Iron and chromium-based oxides for residual methane abatement under realistic conditions: a study on sulfur dioxide poisoning and steam-induced inhibition, *Appl. Catal., B*, 2020, **277**, 119139, DOI: [10.1016/j.apcatb.2020.119139](#).
  - 34 G. C. Chinchén, R. H. Logan and M. S. Spencer, Water-gas shift reaction over an iron oxide/chromium oxide catalyst, *Appl. Catal.*, 1984, **12**(1), 89–96, DOI: [10.1016/s0166-9834\(00\)81506-7](#).
  - 35 F. Meshkani, M. Rezaei and M. Jafarbegloo, Preparation of nanocrystalline Fe<sub>2</sub>O<sub>3</sub>–Cr<sub>2</sub>O<sub>3</sub>–CuO powder by a modified urea hydrolysis method: a highly active and stable catalyst for high temperature water gas shift reaction, *Mater. Res. Bull.*, 2015, **64**, 418–424, DOI: [10.1016/j.materresbull.2014.12.038](#).
  - 36 M. I. Baraton, G. Busca, M. C. Prieto, G. Ricchiardi and V. Sanchez Escribano, On the Vibrational Spectra and Structure of FeCrO<sub>3</sub> and of the Ilmenite-Type Compounds CoTiO<sub>3</sub> and NiTiO<sub>3</sub>, *J. Solid State Chem.*, 1994, **112**(112), 9–14.
  - 37 D. Renusch, B. Veal, K. Natesan and M. Grimsditch, Transient oxidation in Fe–Cr–Ni alloys A Raman-scattering study, *Oxid. Met.*, 1996, **46**, 365–381.
  - 38 P. Bhardwaj, J. Singh, R. Kumar, D. Kumar, V. Verma and R. Kumar, Oxygen defects induced tailored optical and magnetic properties of Fe<sub>x</sub>Cr<sub>2–x</sub>O<sub>3</sub>(0≤x≤0.1) nanoparticles, *Appl. Phys. A: Mater. Sci. Process.*, 2022, **128**(2), 135, DOI: [10.1007/s00339-021-05233-x](#).
  - 39 H. K. Mehtani, M. I. Khan, B. N. Jaya, S. Parida, M. J. N. V. Prasad and I. Samajdar, The oxidation behavior of iron-chromium alloys: the defining role of substrate chemistry on kinetics, microstructure and mechanical properties of the oxide scale, *J. Alloys Compd.*, 2021, **871**, 159583, DOI: [10.1016/j.jallcom.2021.159583](#).
  - 40 I. Banerjee, H. K. D. Kim, D. Pisani, K. P. Mohanchandra and G. P. Carman, Magnetic anisotropy and magnetodielectric coefficients in Cr<sub>2</sub>O<sub>3</sub> and Fe<sub>0.4</sub>Cr<sub>1.6</sub>O<sub>3</sub>, *J. Alloys Compd.*, 2014, **614**, 305–309, DOI: [10.1016/j.jallcom.2014.06.038](#).
  - 41 L. Z. Liu, T. H. Li, X. L. Wu, J. C. Shen and P. K. Chu, Identification of oxygen vacancy types from Raman spectra of Sn<sub>2</sub> nanocrystals, *J. Raman Spectrosc.*, 2012, **43**(10), 1423–1426, DOI: [10.1002/jrs.4078](#).
  - 42 X. Yue, L. Zhang, L. Ma, M. Lu, A. Neville and Y. Hua, Influence of a small velocity variation on the evolution of the corrosion products and corrosion behaviour of super <sup>13</sup>Cr SS in a geothermal CO<sub>2</sub> containing environment, *Corros. Sci.*, 2021, **178**, 108983, DOI: [10.1016/j.corsci.2020.108983](#).
  - 43 H.-Y. Lin, Y.-W. Chen and C. Li, The mechanism of reduction of iron oxide by hydrogen, *Thermochim. Acta*, 2003, **400**(1–2), 61–67, DOI: [10.1016/s0040-6031\(02\)00478-1](#).
  - 44 V. V. Kovalenko, M. N. Rumyantseva, A. M. Gaskov, E. V. Makshina, V. V. Yushchenko, I. I. Ivanova, A. Ponzoni, G. Faglia and E. Comini, SnO<sub>2</sub>/Fe<sub>2</sub>O<sub>3</sub> nanocomposites: ethanol-sensing performance and





- catalytic activity for oxidation of ethanol, *Inorg. Mater.*, 2006, **42**(10), 1088–1093, DOI: [10.1134/s0020168506100074](https://doi.org/10.1134/s0020168506100074).
- 45 V. Galvita and K. Sundmacher, Redox behavior and reduction mechanism of  $\text{Fe}_2\text{O}_3$ – $\text{CeZrO}_2$  as oxygen storage material, *J. Mater. Sci.*, 2007, **42**(22), 9300–9307, DOI: [10.1007/s10853-007-1872-7](https://doi.org/10.1007/s10853-007-1872-7).
- 46 Y.-Q. Wang, Y.-X. Li, X. Fu, J.-Y. Yue, J.-W. Cao, X.-B. Ma, F. Liu and J.-W. Wang, Catalytic oxidation of toluene by binary metal oxide  $\text{Cr}_2\text{O}_3/\text{CeO}_2$  from MIL-101 (Cr), *J. Solid State Chem.*, 2023, **328**, 124334, DOI: [10.1016/j.jssc.2023.124334](https://doi.org/10.1016/j.jssc.2023.124334).
- 47 G. Festa, A. Serrano-Lotina, E. Meloni, R. Portela, C. Ruocco, M. Martino and V. Palma, Support Screening to Shape Propane Dehydrogenation SnPt-Based Catalysts, *Ind. Eng. Chem. Res.*, 2024, **63**, 16269–16284, DOI: [10.1021/acs.iecr.3c04089](https://doi.org/10.1021/acs.iecr.3c04089).
- 48 J. Tian, P. Zheng, T. Zhang, Z. Han, W. Xu, F. Gu, F. Wang, Z. Zhang, Z. Zhong, F. Su, *et al.*,  $\text{CO}_2$  methanation over Ni nanoparticles inversely loaded with  $\text{CeO}_2$  and  $\text{Cr}_2\text{O}_3$ : catalytic functions of metal oxide/Ni interfaces, *Appl. Catal., B*, 2023, **339**, 123121, DOI: [10.1016/j.apcatb.2023.123121](https://doi.org/10.1016/j.apcatb.2023.123121).
- 49 Z. Xie, B. Yan, J. H. Lee, Q. Wu, X. Li, B. Zhao, D. Su, L. Zhang and J. G. Chen, Effects of oxide supports on the  $\text{CO}_2$  reforming of ethane over Pt-Ni bimetallic catalysts, *Appl. Catal., B*, 2019, **245**, 376–388, DOI: [10.1016/j.apcatb.2018.12.070](https://doi.org/10.1016/j.apcatb.2018.12.070).
- 50 V. Thapliyal, M. E. Alabdulkarim, D. R. Whelan, B. Mainali and J. L. Maxwell, A concise review of the Raman spectra of carbon allotropes, *Diamond Relat. Mater.*, 2022, **127**, 109180, DOI: [10.1016/j.diamond.2022.109180](https://doi.org/10.1016/j.diamond.2022.109180).

